Quasi-analytical homogenization approach for the non-linear analysis of in-plane loaded masonry panels

by

Gabriele Milani[(1)*], Elisa Bertolesi[(1)]

(1) Department of Architecture, Built environment and Construction engineering ABC
Politecnico di Milano
Piazza Leonardo da Vinci 32, 20133 Milan, Italy
* Corresponding author. E-mail: gabriele.milani@polimi.it. Phone: +39 022399 4225 Fax: +39 022399 4220

Abstract

Keywords: *Masonry; in-plane loads; semi-analytical approach; compatible model of homogenization; holonomic non-linear model.*

A simple holonomic compatible homogenization approach for the non-linear analysis of masonry walls in-plane loaded is presented.
The elementary cell (REV) is discretized with 24 triangular elastic constant stress elements (bricks) and non-linear interfaces (mortar). A holonomic behavior with softening is assumed for mortar joints. It is shown how the mechanical problem in the unit cell is characterized by very few displacement variables and how homogenized stress-strain behavior can be evaluated semi-analytically. At a structural level, it is therefore not necessary to solve a FE homogenization problem at each load step in each Gauss point.
Non-linear structural analyses are carried out on a windowed shear wall, for which experimental and numerical data are available in the literature, with the aim of showing how quite reliable results may be obtained with a limited computational effort.

1. Introduction

Masonry is a traditional composite material obtained by the assemblage of bricks and mortar. The variability of the pattern, the shape and dimension of the blocks, as well as the fragile behavior of the constituent materials, make the simulation of masonry still a very challenging task. The elastic behavior is quite limited because masonry is typically characterized by a reduced, almost vanishing tensile strength. Therefore, numerical models traditionally exhibit a moderate level of complexity, because they are native non-linear. As a matter of fact, either macro- or micro-modeling strategies are adopted to deal with masonry over elasticity.

Macro-modeling substitutes bricks and mortar with a homogeneous, sometimes orthotropic material with softening. Abundant is the literature in this regard, see for instance [1]-[3], with the noticeable example of no-tension material modelling (e.g. [1]), which traditionally was conceived to deal with non-linear problems exhibiting predominant mode I fracture of the joints (e.g. arches or pillars under rocking) and masonries with very good compressive strength, where crushing and orthotropic behavior are not paramount. Macro-modelling allows studying even large scale structures without the need of meshing separately bricks and mortar. It is therefore very convenient where efficient computations on engineering structures are needed. Nevertheless, the calibration of model parameters is typically done by means of comprehensive experimental campaigns. When the level of sophistication of the model increases [2]-[3], to better reproduce anisotropy, post-peak softening in tension and compression and a Mohr-Coulomb shear behavior with compression cap, the number of inelastic parameters grows and the experimental characterization may become costly and cumbersome. Theoretically, such approaches may be capable of adequately estimating the non-linear masonry behavior for an arbitrary load combination, even if some meaningful limitations occur in specific cases (see [4] for a detailed discussion), but in practice the needed experimental data fitting would require –at least in principle- new calibrations case by case.

The alternative micro-modeling is simply characterized by a distinct modelling of mortar joints and blocks at a structural level. The reduction of joints to interfaces [5]-[9] helps in limiting variables, especially in the non-linear range, but the approach still remains computationally very demanding, because bricks and mortar are meshed separately. In order to obtain sufficiently reliable solutions in terms of displacements and stresses, constituent materials should be meshed with more than one element, with the consequent grow of the number of non-linear equations to deal with, even for small masonry panels. Furthermore, the pre-processing phase regarding the model generation is not straightforward. Partitioning methods have been recently proposed to overcome such computational limitations and speed up structural analyses.

For the previous reasons, it can be affirmed that macro-scale computations with FEs [10][11] still remain preferable when non-linear analyses for engineering structures are needed.

In such a scenario, homogenization [12]-[23] may represent a fair compromise between micro- and macro-modelling, because it allows in principle to perform non-linear analyses of engineering interest without a distinct representation of bricks and mortar, but still considering their mechanical properties and the actual pattern at a cell level.

Homogenization (or related simplified approaches) is essentially an averaging procedure performed at a meso-scale on a representative element of volume (REV), which generates the masonry pattern under consideration by repetition.

On the REV, a Boundary Value Problem BVP is formulated, allowing an estimation of the expected average masonry behavior to be used at structural level. As a matter of fact, the resultant material obtained from meso-scale homogenization turns out to be orthotropic, with softening in both tension and compression. A straightforward approach to solve BVPs at the meso-scale is obviously based on FEs [15][20]-[23], where bricks and mortar are either elasto-plastic with softening or damaging materials. It is also known as FE^2 and essentially is a twofold discretization, the first for the unit cell and the second at structural level. However, FE^2 appears still rather demanding, because a new BVP has to be solved numerically for each load step, in each Gauss point.

Alternatively, in this paper, a simplified homogenization two-step model is proposed for the non-linear structural analysis of masonry walls in-plane loaded. The first step is applied at the meso-scale, where the assemblage of bricks and mortar in the REV is substituted with a macroscopic equivalent material through a so called compatible identification, belonging to the wide family of the homogenization procedures. The unit cell is meshed by means of 24 triangular constant stress (CST) plane stress elements (bricks) and interfaces for mortar joints. Triangular elements are assumed linear elastic, whereas the mechanical response of the interface elements includes two dominant deformation modes, namely peel (mode I) and shear (mode II) or a combination of two (mixed mode). Such elements are equipped with a constitutive relationship referred to as

"holonomic" since expressed in terms of normal and tangential tractions σ and τ as a path independent function of the normal and tangential relative displacements at the interface. Both a piecewise linear and an exponential law formally identical to an improved version of the Xu-Needleman law and proposed in another context [24]-[26] are implemented. Such cohesive relationships are characterized by a post-peak softening branch, eventually with a coupling between normal and shear relationships in the case of the improved Xu-Needleman model.

The second step, performed at a structural level, relies into the implementation of the homogenized stress-strain relationships into either a FE code dealing with softening materials (nested multi-scale technique) or a rigid element approach (RBSM) where contiguous rigid elements are connected by shear and normal non-linear homogenized springs.

The first approach (nested multi-scale technique) is very similar to FE^2, but has the advantage that the BVP at the meso-scale level is solved in quasi-analytical form. Limitations of FE^2 are therefore totally superseded, since the solution in terms of displacements and stresses is found at a cell level in a semi-analytical fashion, with an implementation of the routine used at a meso-level to evaluate homogenized quantities directly at a structural level. As a consequence, the scale passage does not require the huge computational effort needed by FE^2.

The second approach (RBSM) has the advantage that meso- and macro-scale are fully decoupled, i.e. homogenized stress-strain non-linear relationships of the springs connecting rigid elements are evaluated in a previous phase, without the need of solving new BVPs at each load step in each Gauss point. The disadvantage of RBSM is the intrinsic mesh dependence of the results in case of global softening.

In both cases, it is worth mentioning that any commercial code can be suitably used for the implementation of the homogenization model proposed.

The procedure is quite efficient and reliable because it is not necessary to discretize with refined meshes the elementary cell (only three kinematic variables are needed at the meso-scale) and hence it is possible to drastically speed up computations. In addition, the holonomic laws assumed for

mortar allow for a total displacement formulation of the model, where the only variables entering into the homogenization problem are represented by displacements.

Notation: Vectors and tensors are indicated in bold. $\mathbf{E}$ and $\mathbf{\Sigma}$ indicate strain and stress homogenized tensors, *x* (*y*) is the horizontal (vertical) in plane direction, E_{xx} ($E_{yy}, E_{xy} = \Gamma_{xy}/2$, E_{nn}) is the macroscopic horizontal (vertical, shear, on direction *n*) strain, Σ_{xx} ($\Sigma_{yy}, T_{\mathrm{hom}}$) is the homogenized horizontal (vertical, shear) stress, $\sigma_{xx}^{(k)}$ ($\sigma_{yy}^{(k)}, \tau^{(k)}$) is the local horizontal (vertical, shear) stress on element *k*, $\varepsilon_{xx}^{(k)}$ ($\varepsilon_{yy}^{(k)}, \varepsilon_{xy}^{(k)} = \gamma_{xy}^{(k)}/2$) is the local horizontal (vertical, shear) strain on element *k*, L (H) is the brick semi-length (height), $\rho = L/2H$, A is the elementary cell (REV) area, $2e_v$ (e_h, e) is head (bed, generic) joint thickness, U_x^0 (U_y^0) indicate an imposed boundary horizontal (vertical) displacement in the biaxial strain problem, U_x^i (U_y^i) is the *i*-th node unknown horizontal (vertical) displacement, Δ_n (Δ_t) is the interface normal (tangential) jump of displacements, $f_n^{I,II}$ ($f_t^{I,II}$) is the joint (I: head, II: bed) normal (shear) stress, $\xi = U_x^0 - U_x^9$, $\eta = U_y^5 + U_y^6$, E_b (ν_b, G_b) is the brick Young modulus (Poisson's ratio, shear modulus), E_m (G_m) is mortar Young (shear) modulus, D_{ijhk} is the homogenized elastic stiffness *ijhk* component, Δ_n^{ul} (Δ_t^{ul}) is the ultimate joint normal (tangential) jump of displacements in the multi-linear model, f_t (c) is joint tensile strength (cohesion), δ_n δ_t ϕ_n and ϕ_t are Xu-Needleman interface parameters, $\xi^t = U_x^5 + U_x^6$, $\eta^t = U_y^3$, $\kappa = \tau^{(1)} e_v / G_b$, $\overline{U}_x^t$ ($\overline{U}_y^t$) indicate an imposed boundary horizontal (vertical) displacement in the shear problem, $\vartheta = \tan^{-1}\left(E_{yy}/E_{xx}\right)$.

2. The simplified (compatible homogenization) holonomic model

One of the basic concepts of homogenization is the utilization of averaged quantities for the macroscopic strain and stress tensors (respectively $\mathbf{E}$ and $\mathbf{\Sigma}$) [15][20]-[22][27] on a representative element of volume *Y* (REV or elementary cell, Figure 1), i.e. $\mathbf{E} = <\boldsymbol{\varepsilon}> = \frac{1}{A}\int_Y \boldsymbol{\varepsilon}(\mathbf{u})dY$ and $\mathbf{\Sigma} = <\boldsymbol{\sigma}> = \frac{1}{A}\int_Y \boldsymbol{\sigma}dY$, where *A* is the area of the elementary cell, $\boldsymbol{\varepsilon}$ and $\boldsymbol{\sigma}$ are local quantities (strains and stresses respectively) and <*> is the averaging operator. Anti-periodicity is imposed on $\boldsymbol{\sigma}$ and periodicity on the displacement field $\mathbf{u}$:

$$\begin{cases} \mathbf{u} = \mathbf{E}\tilde{\mathbf{x}} + \mathbf{u}^{\mathrm{per}} \quad \mathbf{u}^{\mathrm{per}} \text{ on } \partial Y \\ \boldsymbol{\sigma}\mathbf{n} \quad \text{anti - periodic} \quad \text{on } \partial Y \end{cases} \qquad (1)$$

where $\mathbf{u}$ is the total displacement field, $\mathbf{u}^{\text{per}}$ is a periodic displacement field, $\tilde{\mathbf{x}} = \{x \quad y \quad z\}$ is the local frame of reference (see Figure 1) and **E** is the homogenized strain tensor.

In the model proposed, which is a simplified homogenization that will be called from here ongoing "compatible identification" (and already used by one of the authors in [28] but with different material models and a FE implementation), joints are reduced to holonomic zero thickness interfaces and bricks are coarsely discretized with triangular constant stress elastic elements, see Figure 1. It is necessary to mesh 1/4 of the unit cell through at least 6 triangular brick elements, labeled in Figure 1 as (1)-(2)-(3)-(1')-(2')-(3'), in order to suitably reproduce shear stress on the bed joint (element 2) in horizontal stretching. When dealing with the non linear approach presented hereafter [14], all the non-linearity in the REV is therefore concentrated on joints reduced to interfaces. Brick-brick interfaces are assumed not active (i.e. the jump of normal and tangential displacements is assumed to vanish) in order to reduce variables.

Indicating with $\mathrm{o}^{(n)}$ a stress component belonging to the *n*-th element, the stress tensor inside the *n*-th element $\boldsymbol{\sigma}^{(n)}$ is constituted by the components $\sigma_{xx}^{(n)}$ (horizontal stress), $\sigma_{yy}^{(n)}$ (vertical stress) and $\tau^{(n)}$ (shear stress). Equilibrium inside each element is automatically satisfied, $div\boldsymbol{\sigma} = 0$, whereas two equality constraints involving stress tensors of contiguous triangles has to be imposed for each internal interface. In particular, for 1-2 interface, the stress vector (normal and tangential component) must be equal passing from element 1 to element 2, i.e. $\sigma_{xx}^{(2)} = \sigma_{xx}^{(1)} + \rho\left(\tau^{(1)} - \tau^{(2)}\right)$ and $\sigma_{yy}^{(2)} = \sigma_{yy}^{(1)} + \rho^{-1}\left(\tau^{(1)} - \tau^{(2)}\right)$, with ρ defined as the ratio between the semi-length of the bricks and its height, i.e. $\rho = L/2H$. Analogous equations can be written for 3-2, 3'-2', 2-2' and 2'-1' interfaces.

Assuming that the triangular elements are linear elastic, the following relationship in Voigt notation between strains and stresses can be written:

$$\begin{bmatrix} \varepsilon_{xx} \\ \varepsilon_{yy} \\ \gamma_{xy} \end{bmatrix} = \begin{bmatrix} \dfrac{\sigma_{xx}}{E_b} - \dfrac{\nu_b \sigma_{yy}}{E_b} \\ -\dfrac{\nu_b \sigma_{xx}}{E_b} + \dfrac{\sigma_{yy}}{E_b} \\ \dfrac{\tau}{G_b} \end{bmatrix} \qquad (2)$$

Where E_b, ν_b and G_b are block elastic modulus, Poisson's ration and shear modulus, respectively.

The semi-analytical approach proposed in the paper for the compatible homogenization of running bond masonry is therefore constituted by elastic triangular elements at constant stress and strain fields and all non-linearity concentrated on joints reduced to interfaces. Interfaces non-linear behavior is holonomic, which appears suitable for non-linear static analysis of masonry elements.

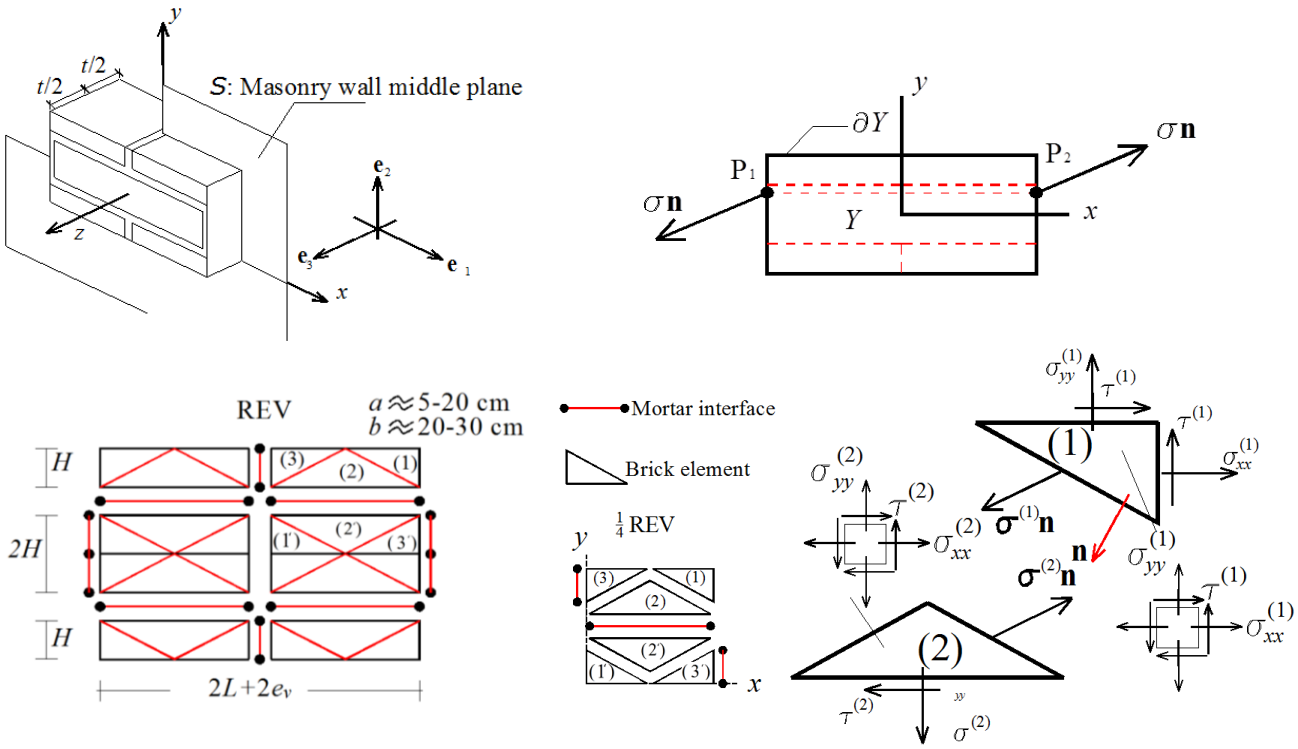

Figure 1: The compatible homogenization presented. REV mesh with 24 CST brick elastic elements and holonomic mortar interfaces. Anti-periodicity of the micro-stress field.

2.1. Holonomic relationships for mortar joints reduced to interfaces

Under mixed-mode loading conditions, expected to occur in mortar joints, two interface relationships, in a sense alternative, are considered in what follows and comparatively assessed. (a) A multi-linear relationship, including at a first attempt normal and tangential responses completely

independent on each other (de-coupled approach), i.e. $\sigma_n(\Delta_n)$ and $\tau(\Delta_t)$. Although not fully realistic, this approach is very straight-forward and allows for an impressive stability and rapid convergence of the algorithms. As an alternative, the cohesive relationship at the previous point (i) can be modified to take into account the frictional behavior among bricks. In this case the peak tangential stress $\tau_{\lim}$ is assumed to depend on the current normal stress level at the interface σ_n by a classic Mohr-Coulomb criterion, namely $\tau_{lim} = -\sigma_n + c\tan\varphi$, where$\tau_{\lim}$ φ and c denotes the friction angle and the cohesion, respectively. This choice may be useful to describe frictional sliding among the bricks. (b) The second choice is an improved version of the Xu–Needleman exponential law [24]-[26], hereafter called simply "Xu-Needleman" for the sake of conciseness. In this law the stress vector $\left[\sigma_n \quad \tau\right]^T$ at the interface is given the following closed-form expression:

$$\begin{aligned}\sigma_n &= \frac{\varphi_n}{\delta_n}\left(\frac{\Delta_n}{\delta_n}\right)e^{-\left(\frac{\Delta_t}{\delta_t}\right)^2}e^{-\frac{\Delta_n}{\delta_n}}\\ \tau &= 2\frac{\varphi_t}{\delta_t}\left(\frac{\Delta_t}{\delta_t}\right)\left(1+\frac{\Delta_n}{\delta_n}\right)e^{-\left(\frac{\Delta_t}{\delta_t}\right)^2}e^{-\frac{\Delta_n}{\delta_n}}\end{aligned} \qquad (3)$$

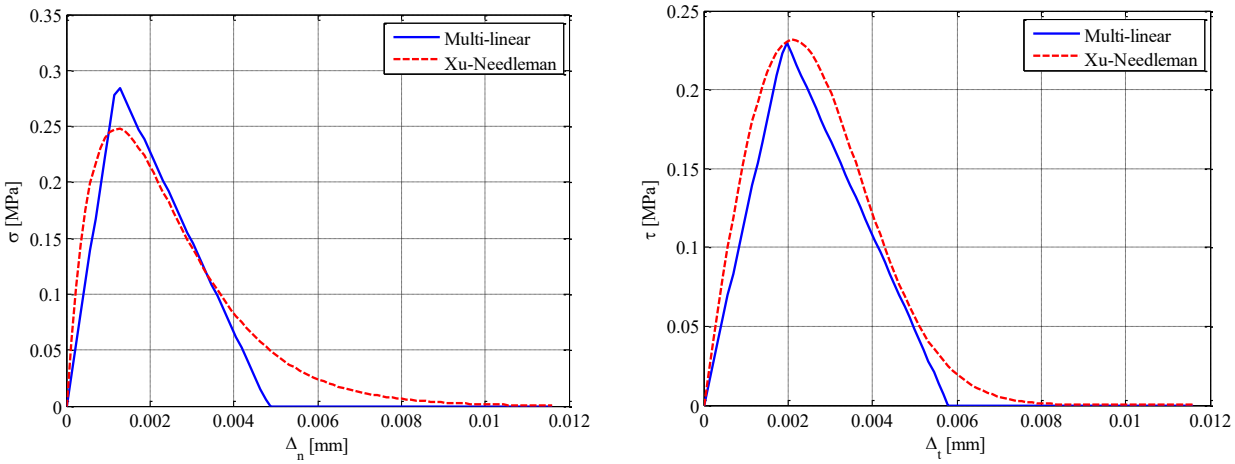

Figure 2: Qualitative comparison between multi-linear and Xu-Needleman relationships adopted in the paper to model non-linear behavior of mortar joints under normal actions (left) and shear (right).

Symbols ϕ_n and ϕ_t denote the work of separation under pure Mode I (i.e. when $\Delta_t = 0$) and Mode II (i.e. when $\Delta_n = 0$), respectively, while δ_n and δ_t indicate the relevant characteristic lengths. It is interesting to point out that Eq. (3) may or may not derive from a potential, but still remains

holonomic, i.e. expressed in terms of jumps of displacements instead of increments. There is no unloading rule to define, meaning that load-unload paths are the same, making therefore the approach unsuited for non-linear dynamics. In order to extend the model to non-linear dynamic loads, a damage plasticity model fitting homogenization curves at a structural level should be used.

It is also worth emphasizing that equations (3) imply a strongly coupled response: softening occurs for both the tractions although the interface is being stressed along one direction only. In compression the response of mortar joints is assumed to be linear elastic until the interpenetration constraint is activated through a very high stiffness, acting as a penalty factor. Whilst there is theoretically the possibility to model masonry crushing, this matter goes beyond the scopes of the present paper, because would involve bricks failure and 3D effects, not easily reproducible with simplified approaches. A qualitative comparison of the two models investigated is provided in Figure 2.

2.2. The numerical model in the non-linear range

For the computations, reference is made to the general approach called “compatible identification”, proposed by one of the authors in e.g. [28] to solve the homogenization problem in case of rigid blocks. Roughly it consists in applying a priori-assumed deformation modes on the boundary of the unit cell, deduced from the application of non-null components (one or more) of the homogenized strain tensor and in the subsequent derivation of the homogenized stress tensor.

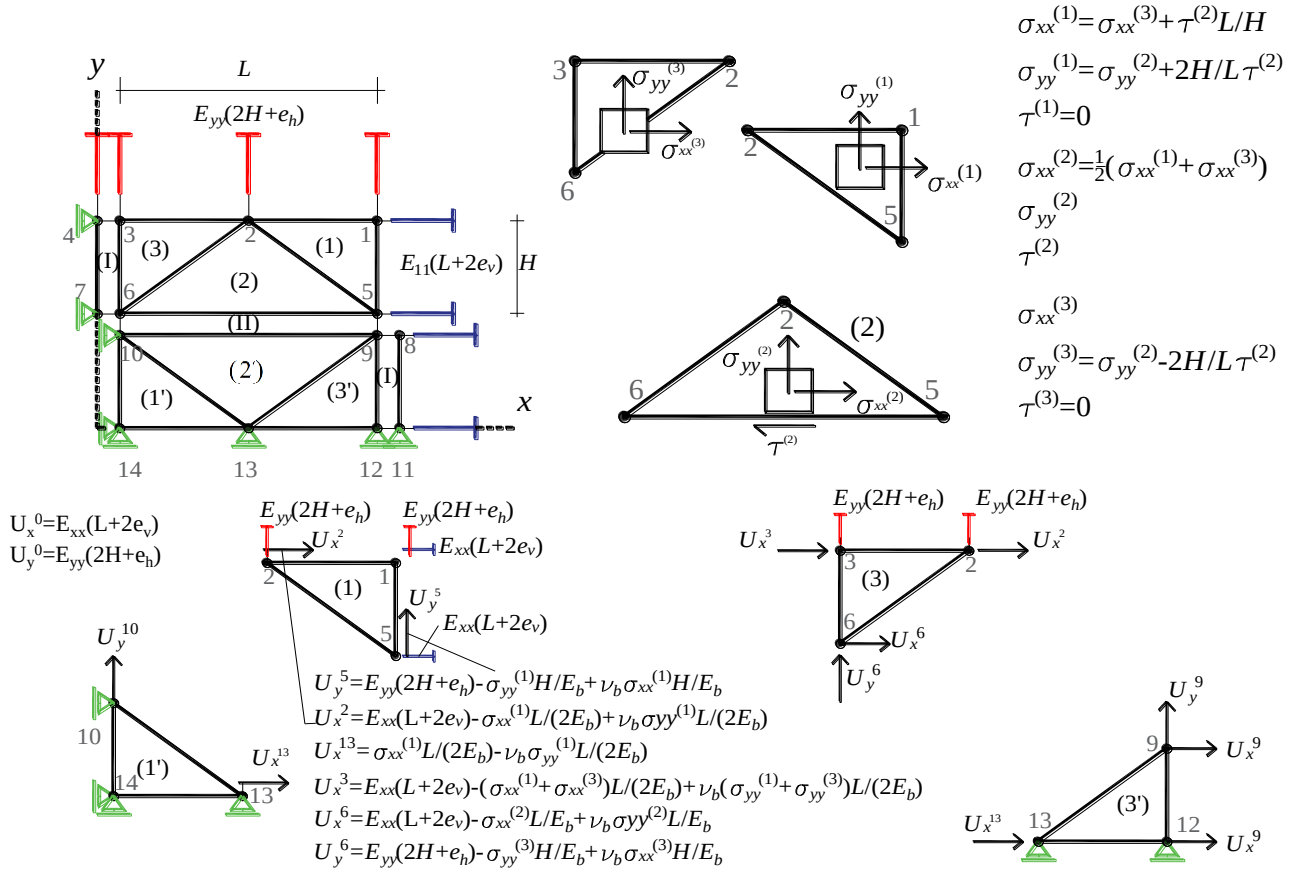

Figure 3: Biaxial stress state problem.

In case of rigid blocks and mortar joints reduced to interfaces, the deduction of stresses acting on interfaces is very straightforward, whereas in case of deformable bricks a FE non-linear problem should be solved.

From here ongoing, the symbols indicated in Figure 3 will be used.

2.2.1. Horizontal stretching ($E_{xx} \neq 0$)

Under the application of the single $E_{xx} \neq 0$ component of the homogenized strain tensor, only ¼ of the unit cell can be considered, with the behavior of elements (3'), (2') and (1') equal to those of elements (3), (2) and (1) respectively. Under such assumptions, it is possible to write both equilibrium and compatibility equations. For instance, when dealing with horizontal equilibrium of element (1), it can be written $\sigma_{xx}^{(1)} = \sigma_{xx}^{(3)} + \tau^{(2)} \frac{L}{H} = f_n^I \left(U_x^0 - U_x^9\right) + f_t^{II} \left(U_x^0 - U_x^9, U_y^5 + U_y^6\right) \frac{L}{H}$, where U_x^0 is the applied boundary displacement, which depends on the assumed homogenized strain E_{xx},

according to a compatible identification procedure, $f_{n,t}^{I,II}$ is the head (*I*) or bed (*II*) joint stress-displacement jump holonomic function along either the normal (*n*) or tangential (*t*) direction, U_x^i (U_y^i) is the horizontal (vertical) displacement of the *i*-th node. The other equilibrium equations – conceptually very similar- are omitted for the sake of conciseness.

Horizontal compatibility written along nodes 1, 2 and 3, remembering that the behavior of the triangular elements is elastic, leads to the equation $U_x^0 - U_x^9 = U_x^0 - \frac{\sigma_{xx}^{(1)}}{E_b}\frac{L}{2} + \frac{\nu_b \sigma_{yy}^{(1)}}{E_b}\frac{L}{2} - \frac{\sigma_{xx}^{(3)}}{E_b}\frac{L}{2} + \frac{\nu_b \sigma_{yy}^{(3)}}{E_b}\frac{L}{2}$ where E_b is the brick elastic modulus and ν_b the Poisson's ratio.

Vertical compatibility written on nodes 3-6 and 1-5, after suitable averaging leads to the following equation: $U_y^5 + U_y^6 + \frac{\sigma_{yy}^{(1)}}{E_b}H - \frac{\nu_b \sigma_{xx}^{(1)}}{E_b}H + \frac{\sigma_{yy}^{(3)}}{E_b}H - \frac{\nu_b \sigma_{xx}^{(3)}}{E_b}H = 0$.

Substituting equilibrium equations into compatibility equations, after suitable rearrangement and with the positions $\xi = U_x^0 - U_x^9$ and $\eta = U_y^5 + U_y^6$, leads to the following system of equations:

$$\begin{aligned} &\text{(a)} \quad \xi = U_x^0 - \frac{L}{E_b} f_n^I(\xi) - \frac{L^2}{2HE_b} f_t^{II}(\xi,\eta) + \frac{\nu_b L}{E_b} f_n^{II}(\xi,\eta) \\ &\text{(b)} \quad \eta + \frac{2H}{E_b} f_n^{II}(\xi,\eta) - \frac{2\nu_b H}{E_b} f_n^I(\xi) - \frac{\nu_b L}{E_b} f_t^{II}(\xi,\eta) = 0 \end{aligned} \qquad (4)$$

It is interesting to notice that when $f_t^{II} = f_t^{II}(\xi)$ and $f_n^{II} = f_n^{II}(\eta)$, then equation (4) reduces to $\xi = U_x^0 - \frac{L}{E_b} f_n^I(\xi) - \frac{L^2}{2HE_b} f_t^{II}(\xi) + \frac{\nu_b L}{E_b} f_n^{II}(\eta)$ and $\eta = -\frac{2H}{E_b} f_n^{II}(\eta) + \frac{2\nu_b H}{E_b} f_n^I(\xi) + \frac{\nu_b L}{E_b} f_t^{II}(\xi)$.

After proper manipulation, the following equations are further obtained:

$$\begin{aligned} &\text{(a) Curve I } \eta = g(\xi): \quad \eta = \frac{2H}{\nu_b L}\left[U_x^0 - \xi - L\frac{1-\nu_b^2}{E_b} f_n^I(\xi) - \frac{L^2}{2H}\frac{1-\nu_b^2}{E_b} f_t^{II}(\xi)\right] \\ &\text{(b) Curve II } \xi = f(\eta): \quad \xi = U_x^0 + \frac{L}{2\nu_b H}\left[-\eta - 2\frac{1-\nu_b^2}{E_b} H f_n^{II}(\eta)\right] \end{aligned} \qquad (5)$$

(5) is a system of non-linear equations that can be solved graphically as follows, see also Figure 4:

1) Assign a value for ξ in equation (5)(a) and find immediately the corresponding value of η. Curve (5)(a) can thus be plotted in the ξ-η plane selecting a suitable range for ξ. Since ξ is the tangential jump of displacements of the horizontal joint, typically the range to inspect is $\xi \in \left[0 \quad \Delta_t^{ul}\right]$, where Δ_t^{ul} is the ultimate tangential jump of displacement of the interface.
2) Assign a value for η in equation (5)(b) and find immediately the corresponding value of ξ. Similarly to Curve I, Curve (5)(b) can thus be plotted in the ξ-η plane selecting a suitable range for η. Again, since η is the normal jump of displacements of the horizontal joint, the range to inspect is $\eta \in \left[0 \quad \Delta_n^{ul}\right]$, where Δ_n^{ul} is the ultimate normal jump of displacement of the interface.
3) The intersection between Curve I and Curve II allows the graphical determination of ξ-η values.

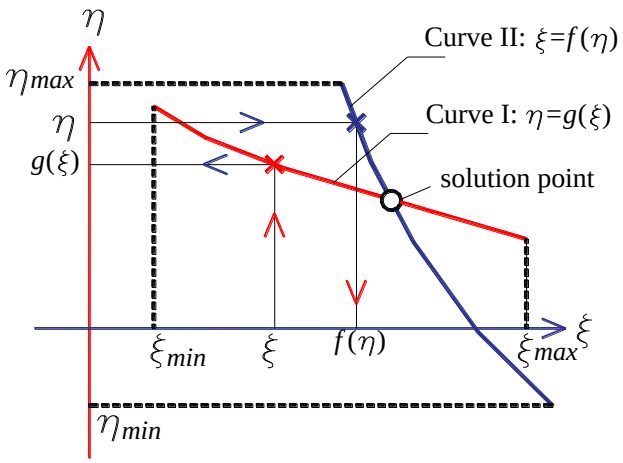

Figure 4: Graphical solution in the biaxial strain state.

When shear and normal behaviors of the interfaces are coupled, analogous relations are derived:

$$\text{(a)} \quad \eta = \frac{2H}{\nu_b L}\left[U_x^0 - \xi - L\frac{1-\nu_b^2}{E_b} f_n^I(\xi) - \frac{L^2}{2H}\frac{1-\nu_b^2}{E_b} f_t^{II}(\xi,\eta)\right]$$

$$\text{(b)} \quad \xi = U_x^0 + \frac{L}{2\nu_b H}\left[-\eta - 2\frac{1-\nu_b^2}{E_b} H f_n^{II}(\xi,\eta)\right] \qquad (6)$$

In this latter case, however, the graphical procedure to determine the solution point is slightly more cumbersome and requires a recursive approach as follows:

1) Assign a value for ξ in equation (6)(a) with η=0 in $f_t^{II}(\xi,\eta)$ and find an updated value for η, say η^i. Put η^i into $f_t^{II}(\xi,\eta)$ and, through (6)(a), estimate again $\eta=\eta^{i+1}$. Repeat until $\eta^i \approx \eta^{i+1}$. Curve (5)(a) is thus plotted in the ξ-η plane within the range $\xi \in [0 \quad \Delta_t^{ul}]$.

2) Assign a value for η in equation (6)(b) with ξ=0 and find an updated value for $\xi=\xi^i$. Put ξ^i into $f_n^{II}(\xi,\eta)$ and estimate a new $\xi=\xi^{i+1}$ by means of (6)(b). η range to inspect is again $[0 \quad \Delta_n^{ul}]$.

3) ξ-η values are estimated at the intersection between Curve I and Curve II.

It is interesting to notice that, when brick Poisson's ratio ν_b=0, it can be shown that $\eta=0$ and system of equations (4) may be re-written as:

$$\begin{aligned} y_1 &= \xi - U_x^0 \\ y_2 &= -\frac{L}{E_b} f_n^I(\xi) - \frac{L^2}{2HE_b} f_t^{II}(\xi) \end{aligned} \qquad (7)$$

With solution $y_1 = y_2$. y_1 is a straight line (with slope equal to 45°) in the $y-\xi$ plane, whereas y_2<0 for ξ>0. According to the graphical procedure proposed in Figure 5, it is very straightforward to find U_x^0 at each assigned ξ.

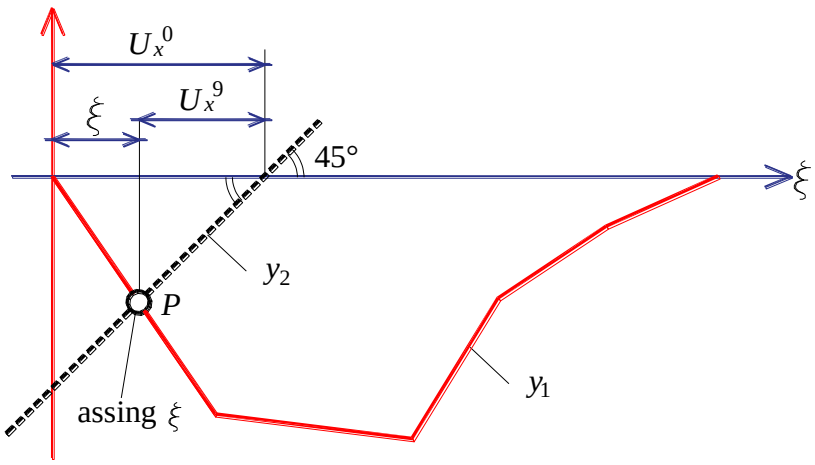

Figure 5: Graphical solution in case of brick Poisson ratio ν_b=0 and U_y^0.

2.2.2. Biaxial strain state ($E_{xx} \neq 0$, $E_{yy} \neq 0$)

When a biaxial strain state is applied to the unit cell, i.e. with both $E_{xx} \neq 0$ and $E_{yy} \neq 0$, it can be shown that equations (5) slightly modifies into:

$$\begin{aligned} &\text{(a) Curve I } \eta = g(\xi): \ \eta = U_y^0 + \frac{2H}{\nu_b L}\left[U_x^0 - \xi - L\frac{1-\nu_b^2}{E_b} f_n^I(\xi) - \frac{L^2}{2H}\frac{1-\nu_b^2}{E_b} f_t^{II}(\xi)\right] \\ &\text{(b) Curve II } \xi = f(\eta): \ \xi = U_x^0 + \frac{L}{2\nu_b H}\left[U_o^y - \eta - 2\frac{1-\nu_b^2}{E_b} H f_n^{II}(\eta)\right] \end{aligned} \qquad (8)$$

where U_y^0 is an applied vertical boundary displacement, representing $E_{yy} \neq 0$, according to the compatible identification procedure adopted.

The solution strategy for the non-linear system of equations (8) is identical to that adopted for problem (6).

2.2.3. Shear behavior ($\Gamma_{xy} \neq 0$)

When dealing with the application, by means of the compatible identification approach adopted, of a macroscopic tangential deformation $\Gamma_{xy} = E_{xy} + E_{yx} \neq 0$, the equilibrated state of stress acting on ¼ of the unit cell is the following (the reader is also referred to Figure 6 for symbols meaning):

$$\begin{aligned} \boldsymbol{\sigma}^{(1)} &= \begin{bmatrix} 0 & \tau^{(1)} \\ \tau^{(1)} & 0 \end{bmatrix} \\ \boldsymbol{\sigma}^{(2)} &= \begin{bmatrix} \dfrac{\tau^{(1)} - \tau^{(3)}}{2}\dfrac{L}{2H} & \dfrac{\tau^{(1)} + \tau^{(3)}}{2} \\ \dfrac{\tau^{(1)} + \tau^{(3)}}{2} & \dfrac{\tau^{(1)} - \tau^{(3)}}{2}\dfrac{H}{2L} \end{bmatrix} \\ \boldsymbol{\sigma}^{(3)} &= \begin{bmatrix} 0 & \tau^{(3)} \\ \tau^{(3)} & 0 \end{bmatrix} \end{aligned} \qquad (9)$$

Where $\boldsymbol{\sigma}^{(i)}$ is the Cauchy stress tensor of the (i)-th element.

After a trivial rearrangement of elements equilibrium equations (not reported here for the sake of conciseness), and with the positions $U_x^5 + U_x^6 = \xi^t$, $U_y^3 = \eta^t$, $E_{xy}(2H + e_h) = \overline{U}_x^t$, $E_{yx}(L + 2e_v) = \overline{U}_y^t$, $\dfrac{\tau^{(1)} e_v}{G_b} = \kappa$, the following equations hold:

$$\text{(a)}\ \xi^t = 2\bar{U}_x^t - \frac{H}{G_b}\left[-\frac{\bar{U}_y^t - \eta^t}{L/2}G_b + 2f_t^I(\eta^t) - \frac{4H}{L}f_n^{II}(\eta^t - \kappa) + 2\frac{\kappa}{L}G_b\right]$$

$$\text{(b)}\ \eta^t = \bar{U}_y^t - \frac{L}{2G_b}\left[2f_t^{II}(\xi^t - \bar{U}_x^t) - \frac{2\bar{U}_x^t - \xi^t}{H}G_b + 2\frac{\kappa}{L}G_b\right] \qquad (10)$$

$$\text{(c)}\ \kappa = \frac{e_v}{G_b}\left[2f_t^{II}(\xi^t - \bar{U}_x^t) - f_t^I(\eta^t)\right]$$

It is interesting to notice that (10) is a system of non-linear equations of three variables ξ^t, η^t and κ.

Assuming an iterative scheme and starting with κ=0, equations (10)(a) and (b) allow for graphical solution (because they are functions of independent variables η^t and ξ^t respectively), similar to that found for the biaxial stress state, see the previous section.

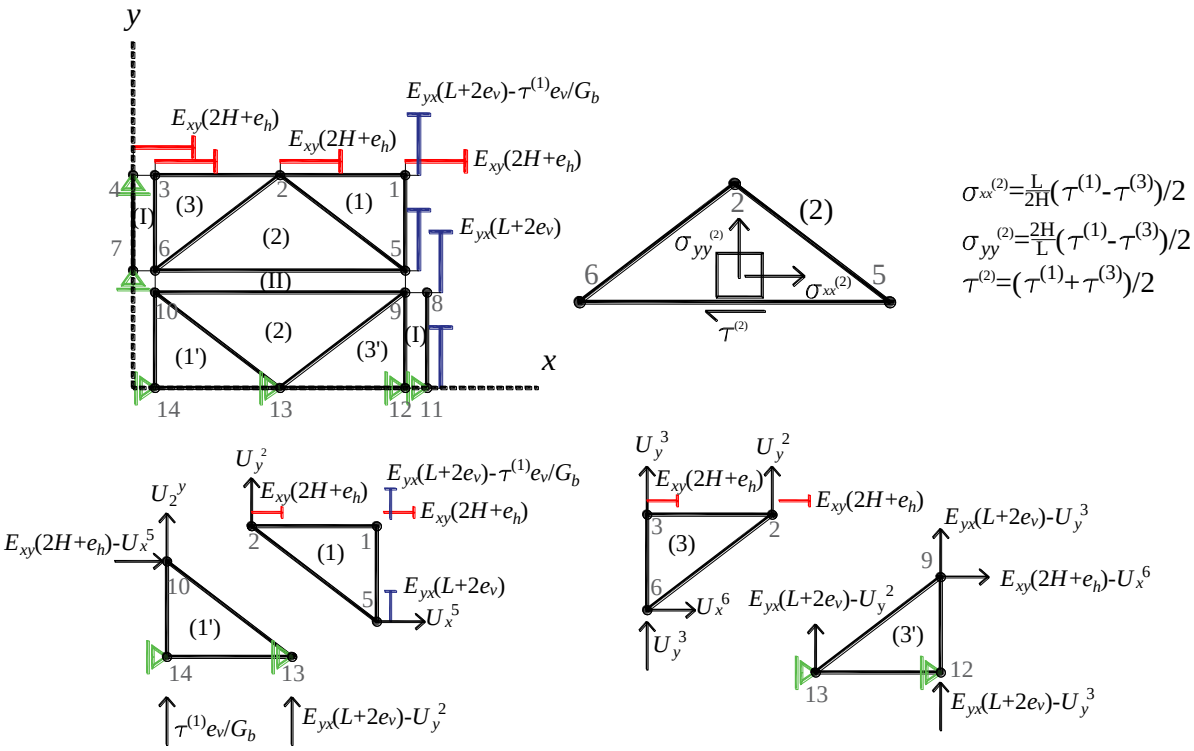

Figure 6: Shear problem, displacement and stress variables.

Equation (10)(c), with the values of η^t and ξ^t found in the solution point provides an updated κ and the procedure is repeated ad libitum. Finally, with the converged solution values of η^t, ξ^t and

κ, displacements U_y^2 and U_x^5 (or U_x^6) are trivially found from equilibrium and compatibility equations.

2.3. Masonry elastic moduli

In case of linear elastic behavior of the interfaces $f_n^I(\xi) = \xi E_m / e_v$, $f_t^{II}(\xi) = \xi G_m / e_h$ and $f_n^{II}(\eta) = \eta E_m / e_h$.

Consequently, equations (8) modify as $\eta = U_y^0 + \frac{2H}{\nu_b L}\left[U_x^0 - \xi - L\frac{1-\nu_b^2}{E_b}\xi\frac{E_m}{e_v} - \frac{L^2}{2H}\frac{1-\nu_b^2}{E_b}\xi\frac{G_m}{e_h}\right]$ and

$\xi = U_x^0 + \frac{L}{2\nu_b H}\left[U_o^y - \eta - 2\frac{1-\nu_b^2}{E_b}H\eta\frac{E_m}{e_h}\right]$.

After trivial algebra, the following system of equations is obtained:

$$\begin{bmatrix} \frac{2H}{\nu_b L} + \frac{2H}{e_v}\frac{1-\nu_b^2}{\nu_b}\frac{E_m}{E_b} + \frac{L}{e_h}\frac{1-\nu_b^2}{\nu_b}\frac{G_m}{E_b} & 1 \\ 1 & \frac{L}{2\nu_b H} + \frac{L}{e_h}\frac{1-\nu_b^2}{\nu_b}\frac{E_m}{E_b} \end{bmatrix}\begin{bmatrix}\xi \\ \eta\end{bmatrix} = \begin{bmatrix} U_y^0 + \frac{2H}{\nu_b L}U_x^0 \\ U_x^0 + \frac{L}{2\nu_b H}U_o^y \end{bmatrix} \qquad (11)$$

System of equations (11) allows for a fast evaluation of both ξ, η variables and, indirectly, using equilibrium equations on bricks and mortar, internal stress variables. Internal stress variables knowledge allows to directly determine elastic moduli.

Similarly, when dealing with the shear problem, from (10) with a linear elastic behavior of the interfaces ($f_t^{II}\left(\xi^t - \overline{U}_x^t\right) = \left(\xi^t - \overline{U}_x^t\right)G_m / e_h$, $f_t^I(\eta^t) = \eta^t G_m / e_v$, $f_n^{II}(\eta^t - \kappa) = (\eta^t - \kappa)E_m / e_h$), and after trivial algebra, the following system of equations holds:

$$\begin{bmatrix} 1 & \frac{2H}{L} + \frac{2H}{e_v}\frac{G_m}{G_b} - \frac{4H^2}{Le_h}\frac{E_m}{G_b} & \frac{4H^2}{Le_h}\frac{E_m}{G_b} + 2\frac{H}{L} \\ \frac{L}{e_h}\frac{G_m}{G_b} + \frac{L}{2H} & 1 & 1 \\ 2\frac{e_v}{e_h}\frac{G_m}{G_b} & -\frac{G_m}{G_b} & -1 \end{bmatrix}\begin{bmatrix}\xi^t \\ \eta^t \\ \kappa\end{bmatrix} = \begin{bmatrix} 2\overline{U}_x^t + 2\frac{H}{L}\overline{U}_y^t \\ \overline{U}_y^t + \left(\frac{L}{e_h}\frac{G_m}{G_b} + \frac{L}{H}\right)\overline{U}_x^t \\ 2\frac{e_v}{e_h}\frac{G_m}{G_b}\overline{U}_x^t \end{bmatrix} \qquad (12)$$

(12) allows a straightforward evaluation of ξ^t, η^t and κ variables, as well as, through equilibrium, of $\tau^{(1)}$ and $\tau^{(3)}$ stresses, and hence of the homogenized elastic shear modulus.

In order to evaluate the reliability of the micro-mechanical model proposed in the elastic range, the homogenized elastic moduli obtained are benchmarked against FE results that are considered as reference.

A running bond unit cell constituted by common Italian bricks and 10 mm thick mortar joints has been considered, discretizing one fourth of the cell with four-noded elements in plane stress and a medium refinement, as illustrated in Figure 7. Three values of mortar Young modulus have been considered (550, 2200 and 4400 MPa), corresponding to mortars ranging from weak to strong according to the Italian code. Seven values of brick elastic moduli have been considered (5000, 7500 10000, 12500, 15000, 17500, 20000 MPa), in order to investigate the response of the model in presence of either quite deformable or stiff blocks. Bricks Poisson's ratio has been maintained always equal to 0.2.

It is worth noting that similar homogenization approaches in the elastic range can be found in e.g. [17][29]-[34].

The resultant D_{ijhk} homogenized elastic membrane coefficients are depicted in Figure 8. It can be easily deduced that the error against FE results (taken as reference) is always lower than 16%, meaning that reliable predictions of the homogenized elastic coefficients may be obtained with the model proposed, at a fraction of the time needed by standard FE discretizations of the unit cell.

Obviously, the obtained vertical elastic stiffness is almost always superimposable with the FE one, because the deformation mode of the unit cell is a vertical homogeneous stretching of bricks and bed joint. A direct estimation of the stiffness value may be also obtained with the well known procedure proposed by Lourenço [31]. It consists in homogenizing a masonry pillar constituted by two half bricks (of height H) and a joint (of thickness e). Accordingly, it can be regarded as a variation of the procedure by Pande et al. [34] applied to the evaluation of the vertical membrane stiffness exclusively. For this structural system, the vertical flexural rigidity can be shown to read:

$$D_{yyyy} = \frac{H+e}{\left(1-\nu_b^2\right)\frac{H}{E_b}+\left(1-\nu_m^2\right)\frac{e}{E_m}} \tag{13}$$

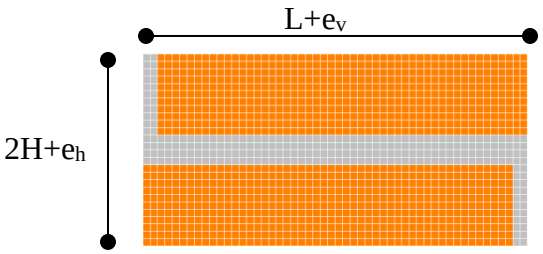

		Geometry	
Brick	2L	250 [mm]	brick length
	2H	55 [mm]	brick height
Mortar	$e_h=2e_v$	10 [mm]	mortar joint thickness

Figure 7: Discretization adopted for the FE simulations on the left, on the right geometry of the unit cell.

Horizontal elastic stiffness is obviously greater than the vertical one, thanks to the contribution in shear of the bed joint. This peculiar behavior is kept by the simplified numerical model, that exhibits on average errors lower than 10% in the wide range of combinations between brick and mortar elastic moduli.

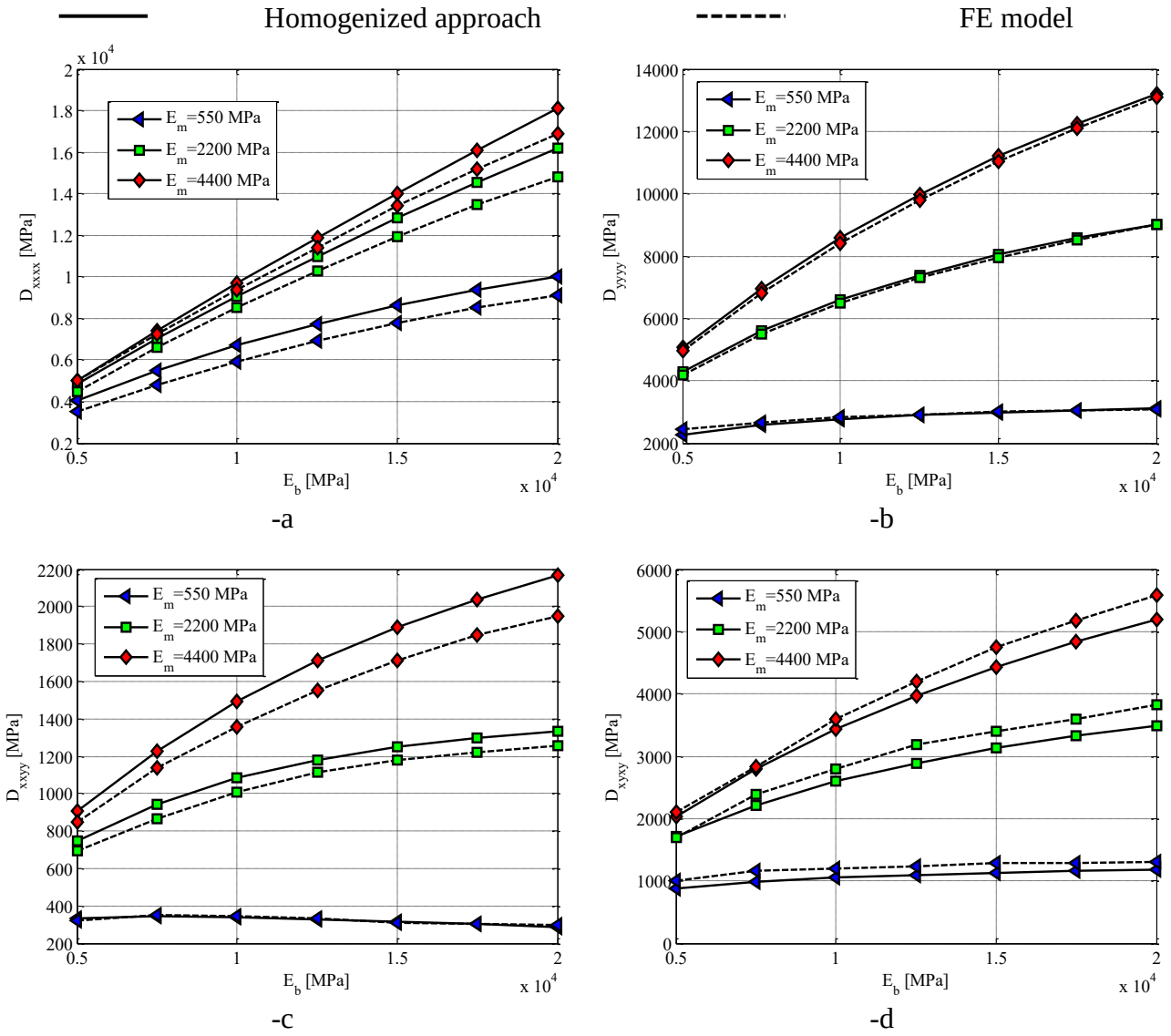

Figure 8: Elastic problem. D_{ijjhk} homogenized moduli obtained with the present model and with FEs at different values of E_b and E_m moduli. –a: D_{xxxx}. –b: D_{yyyy}. –c: D_{xxyy}. –d: D_{xyxy}.

2.4. Numerical simulations at a cell level: inelastic behavior

This section presents some results of numerical simulations at a cell level performed in the inelastic range and obtained by means of the homogenization model proposed. To this aim, a running bond masonry utilized by Raijmakers and Vermeltfoort [39] is considered to test a series of windowed shear walls, constituted of Joosten solid clay bricks (dimensions 210x52x100 mm^3) and 10-mm thick mortar (1:2:9, cement:lime:sand by volume). The same series will be considered at a structural level in the next section, to have an insight into the reliability of the procedure proposed when utilized to predict the non-linear behavior of full scale panels in-plane loaded. Elastic and inelastic material properties are summarized in Table I and are assumed in agreement with those utilized by Lourenço and Rots [5] to perform structural analyses by means of a heterogeneous approach.

Table I: Windowed masonry shear wall by Raijmakers and Vermeltfoort. Mechanical properties assumed for the constituent materials.

Mortar joints (e_h=10 mm)									
Multi-linear model						Xu-Needleman model			
E_m	G_m	f_t	c	Δ_{nu}	Δ_{tu}	ϕ_n	δ_n	ϕ_t	δ_t
[MPa]	[MPa]	[MPa]	[MPa]	[mm]	[mm]	[N/mm]	[mm]	[N/mm]	[mm]
800	$0.4\,E_m$	0.25	$1.35\,f_t$	$6e_h\,f_t/E_m$	$3e_h\,c/G_m$	0.0028	0.0042	0.0060	0.0160
Bricks linear elastic (E_b =16700 MPa, ν_b =0.15)									

The elementary cell is assumed subjected to a biaxial strain state ($E_{xx} \neq 0$, $E_{yy} \neq 0$) and pure shear separately.

When dealing with the biaxial strain state case, E_{xx} and E_{yy} are increased linearly up to the formation of a failure mechanism in the unit cell, keeping the ratio E_{xx}/E_{yy} constant.

The effect of the application of different macroscopic biaxial strain states may be investigated in the model, characterizing the applied strain path by means of the angle ϑ, defined as $\vartheta = \tan^{-1}\left(E_{yy}/E_{xx}\right)$. Three different ϑs are analyzed with both a multi-linear and Xu-Needleman approximation for the mortar joints behavior, namely 0°, 90° and 45°.

ϑ=0° corresponds to the application of a horizontal macroscopic strain, ϑ=90° to a vertical macroscopic strain and ϑ=45° is an intermediate situation where a multi-axial stress state is imposed on the unit cell.

Results obtained for the biaxial strain case are summarized from Figure 9 to Figure 14. In particular Figure 9 and Figure 10 refer to the strain case ϑ=0° (horizontal stretching), Figure 11 and Figure 12 to a vertical stretching ϑ=90° and Figure 13-Figure 14 to an inclined strain state with ϑ=45°. For each ϑ angle, two figures are reported. In the first one (e.g. Figure 11 for ϑ=90°), the strain-homogenized horizontal and vertical stresses Σ_{xx} and Σ_{yy} are depicted in subfigure (-a). In subfigure (-b), strain-horizontal stress curves on elements (1) and (3), i.e. $\sigma_{xx}^{(1)}$ and $\sigma_{xx}^{(3)}$ respectively, and strain-shear stress curves on element (2), i.e. $\tau^{(2)}$, are sketched. Strain-vertical stress curves on elements (1) (2) (3), i.e. $\sigma_{yy}^{(1)}\ \sigma_{yy}^{(2)}\ \sigma_{yy}^{(3)}$ are finally shown in subfigure (–c). In all subfigures, both Xu-Needleman and multi-linear model results are represented.

In the second relevant figure (Figure 10 for ϑ=0° and Figure 12 for ϑ=90°) the following information is provided: subfigures –a and –b show the graphical determination of variables ξ and η at different values of applied macroscopic strains (solution points are identified by blue circles), whereas subfigures –c and –d show values of ξ, η, U_x^9 variables, compared with applied macroscopic strains $U_x^0 = E_{xx}\left(L + 2e_v\right)$ and $U_y^0 = E_{yy}\left(2H + e_h\right)$. Subfigures –a and –c refer to multilinear model, whereas subfigures –b and –d to Xu-Needleman one.

By means of such representations, load cases may be synoptically compared, as well as the response of the unit cell in case of Xu-Needleman and multi-linear behavior of the joints may be evaluated.

From an overall analysis of simulations results, the following considerations may be drawn:

1) The behavior under vertical macroscopic stretching is characterized by the non linear behavior of the bed joint, which fails under pure normal actions, as clearly visible from the deformed shape of Figure 11. It is interesting to notice that the head joint results slightly

loaded, because ξ variable is not always zero during the loading process (see Figure 12) mainly for Poisson's effect on the brick. Figure 12 shows also that η and U_y^0, again for the elastic deformation of the brick, do not coincide. Such a discrepancy justifies the value of the homogenized elastic modulus, which is obviously a weighted average between brick and mortar ones. The graphical solution of problem (5), see also Figure 4, and represented in Figure 12-a &-b for both the multi-linear and Xu-Needleman cases, clearly shows that η monotonically increases, whereas ξ reaches a peak value and then decreases at larger deformations. This is obviously due to the decrease of the stress state within the brick, which obviously corresponds to a decrease of the elastic deformation, and hence of ξ variable. Such conclusion is supported also by the stresses acting on elements (1) and (3), that decrease with the imposed macroscopic deformation and are associated with the elastic strain state of the bricks.

2) The elastic modulus along the vertical direction is 3700 MPa, a value in very good agreement with that used by Pelà and co-workers [40] (3960 MPa) to analyze the same structural problem with an orthotropic macroscopic damage model. The stiffness along the horizontal direction is obviously larger, as it will be discussed in the sequel.
3) Peak strength in vertical stretching is obviously equal to peak joint tensile strength, in both models, see again Figure 11. The post peak behavior is again ruled by bed joint inelastic law. Conversely, the behavior under horizontal stretching is characterized by the formation of tangential actions on element (2), i.e. on the bed joint, see Figure 9. The collapse mechanism of the elementary cell is characterized by shear failure of the bed joint and tensile failure on the head joints, see deformed shape sketched again in Figure 9. Due to the presence of different vertical and horizontal stresses on elements (1) and (3), bricks deformation is non uniform, as it is clearly visible either from the deformed shape or from

vertical (Figure 9-c) and horizontal stresses (Figure 9-b) evolution during the imposed deformation.

4) Peak strength when a horizontal macroscopic strain is applied is obviously much higher than that found in vertical stretching, due to the contribution of the bed joint in shear. Such a result is in perfect agreement with limit analysis considerations, as already shown by many authors, in e.g. [4][12][17][19].

5) When a multi-linear holonomic law for mortar joints is adopted, a homogenized stress-strain curve characterized in the pre-peak range by a roughly bi-linear behavior is observed, see for instance Figure 9-a. When dealing with the Xu-Needleman model in the same figure, the response is obviously smoother, due to the exponential relationships adopted to evaluate tangential and normal stresses on the interfaces. In agreement with intuition, it can be stated that the observed bi-linear (or irregular) response of the homogenized stress-strain curves is linked to the fact that both head and bed joints contribute independently to the homogenized horizontal stress, the first under deformation in pure mode I, and the second under a slightly mixed mode I/mode II. Considering that very small values of η (see Figure 10) are observed, even vanish after the peak stress, it can be stated that in both models the deformation mode of the bed joint when ϑ=0° is almost in pure shear. In light of such considerations, the observed stiffness degradation of the homogenized stress-strain curve within the multi-linear model may be regarded as the activation of non-linearity (more precisely softening) in the bed joint. The average elastic modulus of the homogenized material, intended as the weighted average slope of the bilinear portion of the curve in Figure 9-a is 6314 MPa, is in acceptable agreement with that utilized [40] (7520 MPa).

6) Xu Needleman and multi-linear responses are very similar when the unit cell is deformed separately with a horizontal (ϑ=0°) or a vertical (ϑ=90°) macroscopic strain, with an obvious smoother result found when a Xu-Needleman law is used for joints. However, it is worth noting that, when a biaxial macroscopic strain state is applied, as for instance for ϑ

=45°, the results may be slightly different, as clearly shown in Figure 13. Such a result is not surprising because, when a biaxial macroscopic strain state is applied to the unit cell, joints are generally subjected to both shear and normal actions and, whilst the multi-linear model is fully uncoupled, Xu-Needleman model exhibits strong coupling between σ and τ, see relations (3). In order to find with the Xu-Needleman model a response similar to that obtained with the multi-linear approach with ϑ=45°, it is necessary to considerably reduce the biaxial stress state of the joints. For the case at hand, it is found that when it is assumed ϑ=15°, see results shown in Figure 15, Xu-Needleman model provides results comparable to those provided by the fully uncoupled multi-linear approach subjected to $E_{xx} = E_{yy}$. From the results obtained, it appears clear the intrinsic limitation of a multi-linear fully uncoupled model (which is essentially mono-dimensional), especially in light of its utilization in case of more complex or general loading conditions, which is the typical case of real structure simulations.

Shear behavior according to the proposed model and obeying equations (10), is depicted in Figure 16 and Figure 17 for both the multi-linear and the Xu-Needleman model. In Figure 16, in particular, the homogenized shear strain-shear stress curves are depicted in subfigure –a, whereas the shear stresse curves on elements (1) and (3) are depicted in subfigures –b and –c, respectively. In Figure 17-a and –b the graphical determinations of variables ξ^t and η^t obtained according to equations (10), at different values of applied macroscopic strain are represented (the solution points are identified by blue circles). In addition, in Figure 17-c & -d, values of ξ^t, η^t, U_x^{10}, $\Gamma_{xy} / 2(2H + e_h)$, $\Gamma_{xy} / 2(L + 2e_v)$ are depicted. Deformed shapes of the unit cell at peak values of shear deformation Γ_{xy} are embedded in Figure 16.

From an overall analysis of results obtained with the model proposed subjected to macroscopic shear deformation, both in presence of holonomic multi-linear and Xu-Needleman mortar joints, the following considerations can be drawn:

1) Shear behavior is characterized by the presence of different tangential stresses on elements (1) and (3), clearly visible from the deformed shapes obtained at different increments and from the stress-strain diagrams acting on single elements. Elastic modulus found is equal to 1351 MPa, in very good agreement with literature data and Pelà and co-workers [40] macroscopic numerical model (1460 MPa). The different values of $\tau^{(1)}$ and $\tau^{(3)}$ found (see Figure 16-b & -c are responsible for non null tensile stresses on bed joint, and hence for an axial elongation (or compression) of the joint, again visible from deformed shapes.
2) In agreement with the previous point, η^t variable indicates a jump of displacement normal to the bed joint. It is interesting to notice from Figure 17-a (multi linear) and -b (Xu-Needleman model) that η^t is not null, especially at early deformation stages, say before the peak load is reached. This is clearly evident from deformed shapes represented in Figure 16 where one half of the bed joint undergoes a mixed shear-traction condition, whereas the remaining half a shear-compression condition. After the peak load, η^t decreases and the bed joint tend to flow under pure shear condition. The mixed state of stress experienced on bed joints is also responsible for the different values of tangential stresses observed within brick elements (1) and (3), i.e. $\tau^{(1)}$ and $\tau^{(3)}$, as it is clearly evident from stress-strain output curves depicted in Figure 16.
3) The behaviors (both homogenized stresses and local stresses on single elements) of the multi-linear and Xu-Needleman model result very similar, with obviously a peak strength exclusively ruled by the cohesion assigned to mortar joints.

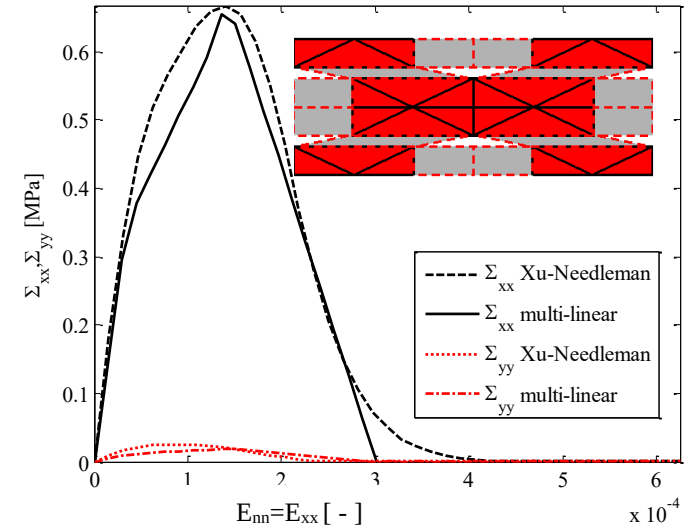

-a

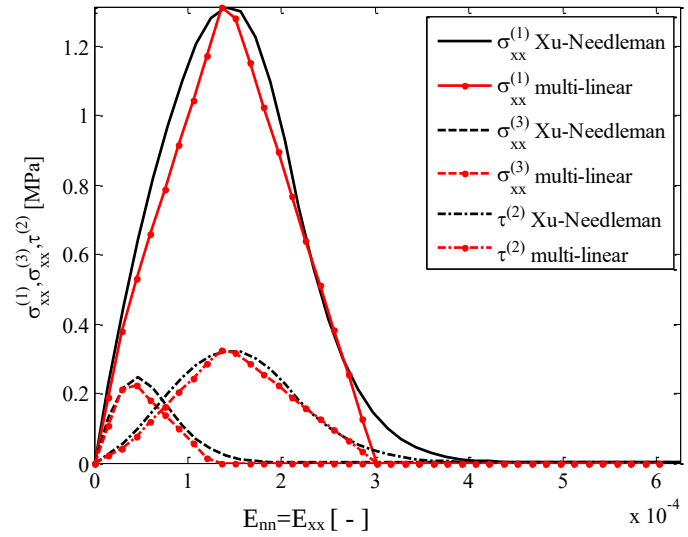

-b

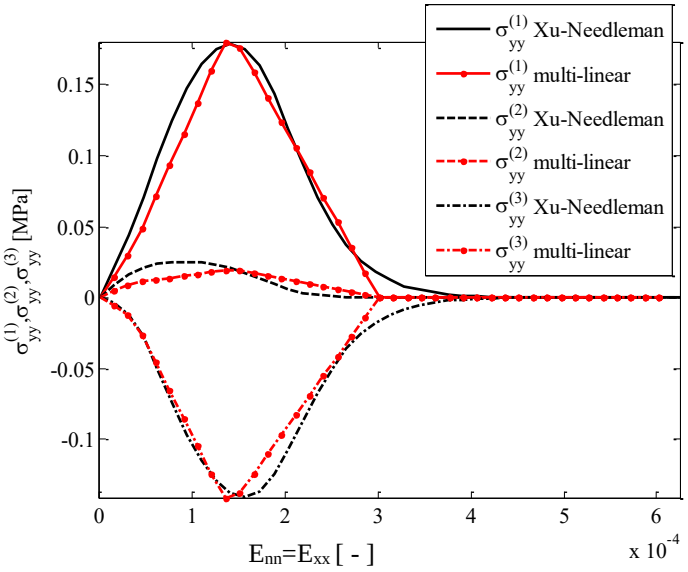

-c

Figure 9: ϑ=0° (horizontal direction of the macroscopic strain). Stress-strain curves. –a: Homogenized horizontal (Σ_{xx}) and vertical (Σ_{yy}) stresses. –b: micro stresses $\sigma_{xx}^{(1)}$, $\sigma_{xx}^{(3)}$, $\tau^{(2)}$. –c: micro stresses $\sigma_{yy}^{(1)}$, $\sigma_{yy}^{(2)}$, $\sigma_{yy}^{(3)}$.

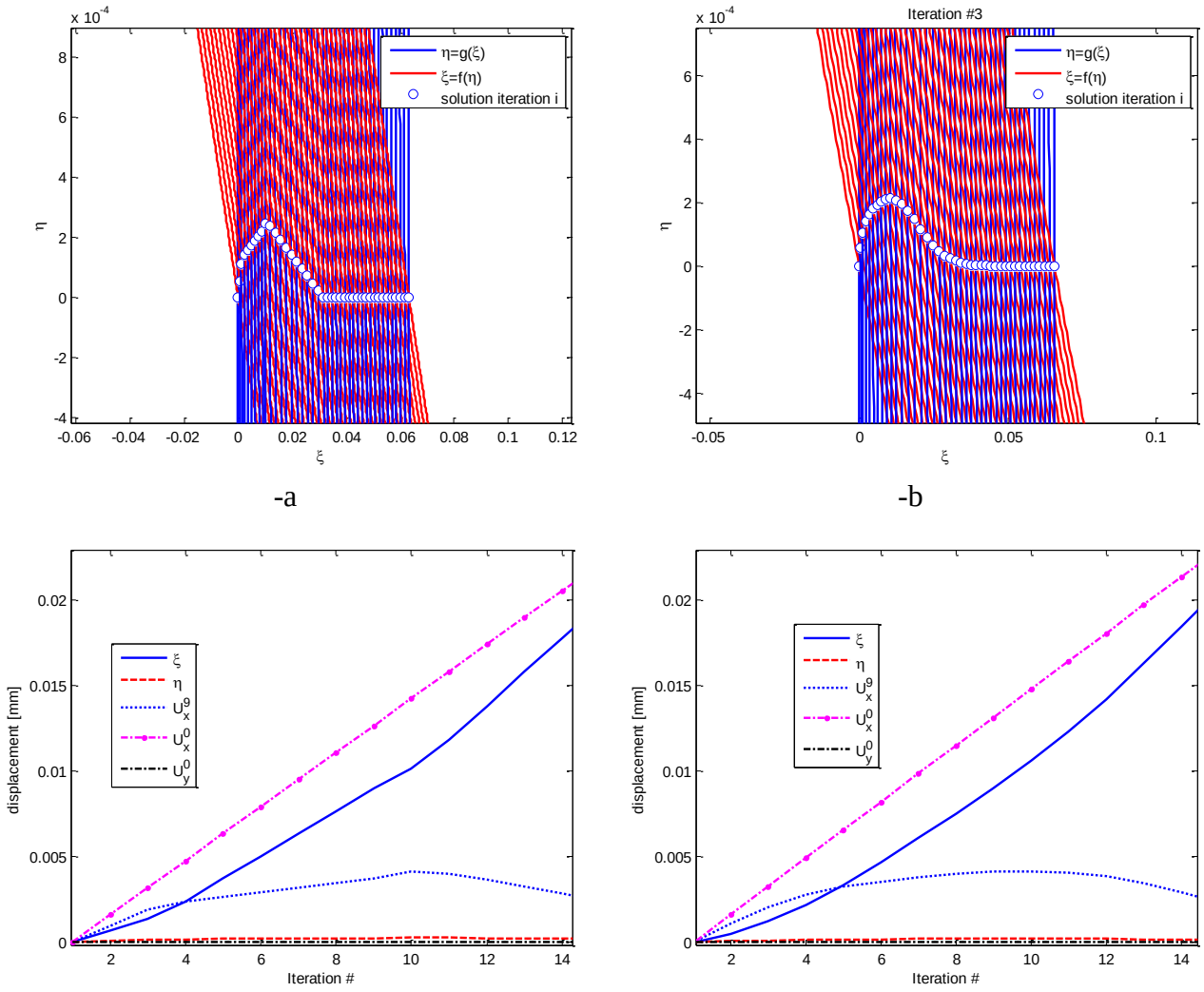

-a -b

-c -d

Figure 10: ϑ=0° (horizontal direction of the macroscopic strain). Graphical determination of variables ξ and η at different values of applied macroscopic strain. –a and -b: $\xi = f(\eta)$ and $\eta = g(\xi)$ functions. –c and -d: values of ξ, η, U_x^9, $U_x^0 = E_{xx}(L + 2e_v)$, $U_y^0 = E_{yy}(2H + e_h)$. –a and –c: multi-linear model. –b and –d: Xu-Needleman model.

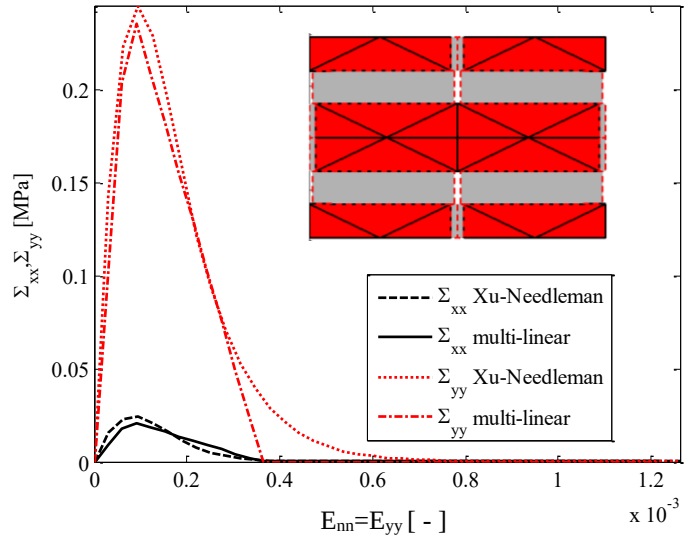

-a

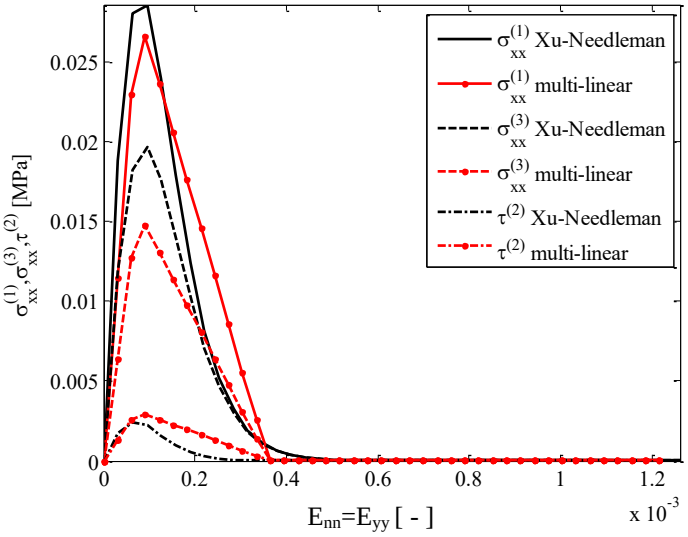

-b

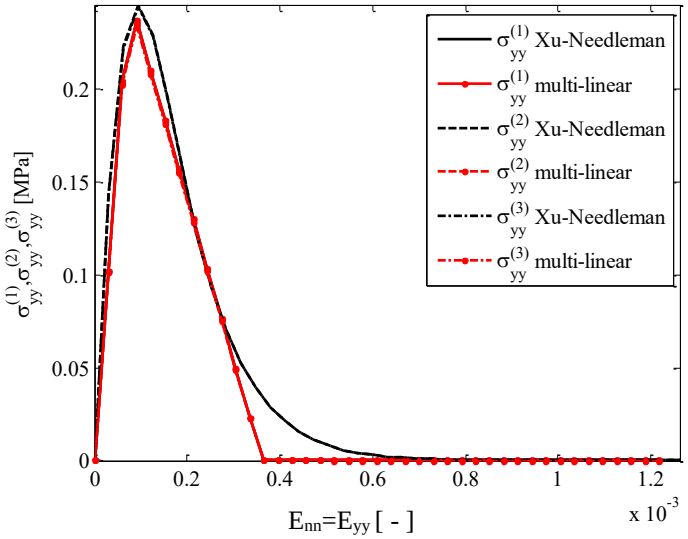

-c

Figure 11: ϑ=90° (vertical direction of the macroscopic strain). Stress-strain curves. –a: Homogenized horizontal (Σ_{xx}) and vertical (Σ_{yy}) stresses. –b: micro stresses $\sigma_{xx}^{(1)}$, $\sigma_{xx}^{(3)}$, $\tau^{(2)}$. –c: micro stresses $\sigma_{yy}^{(1)}$, $\sigma_{yy}^{(2)}$, $\sigma_{yy}^{(3)}$.

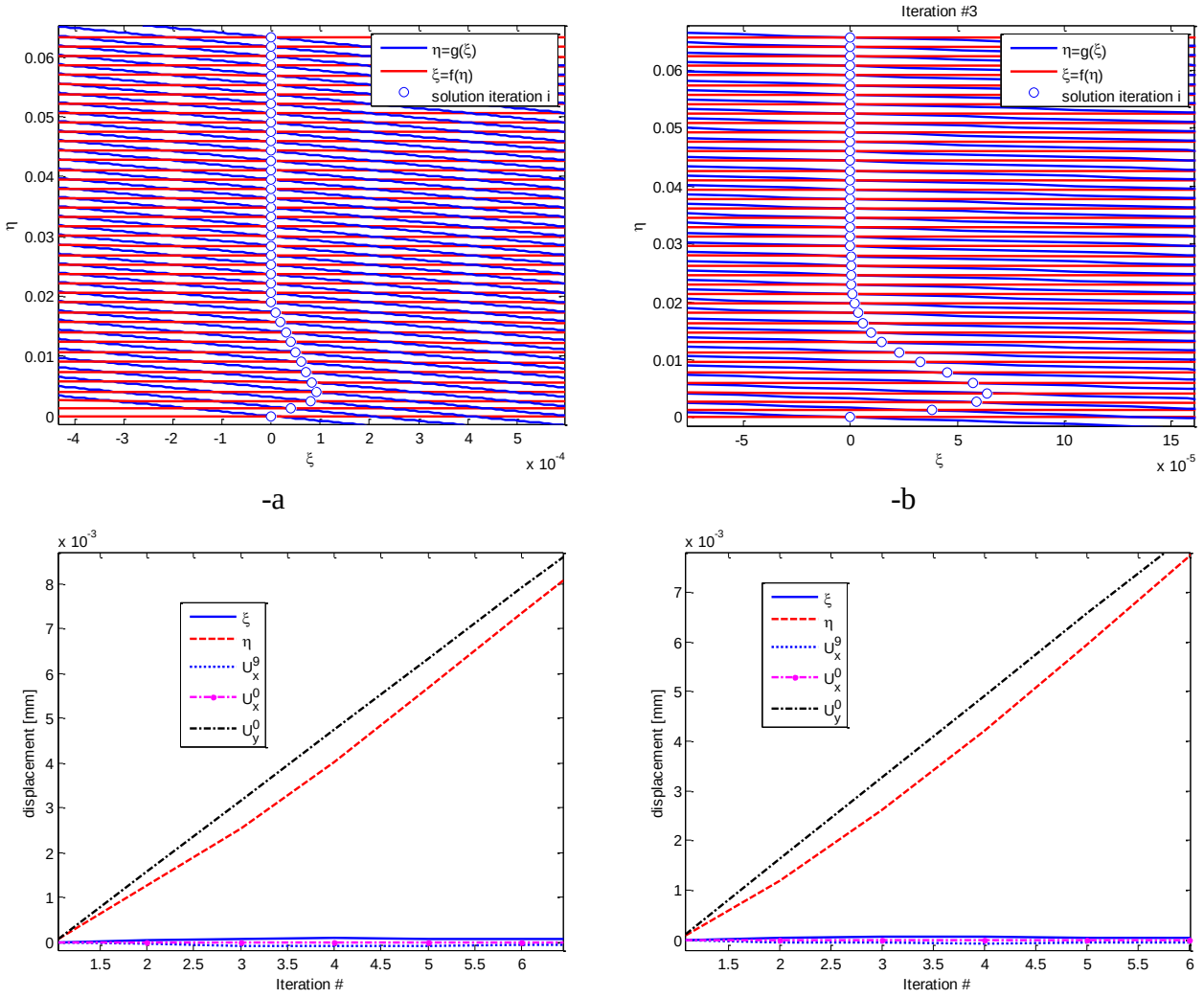

-a -b

-c -d

Figure 12: ϑ=90° (vertical direction of the macroscopic strain). Graphical determination of variables ξ and η at different values of applied macroscopic strain. –a and -b: $\xi = f(\eta)$ and $\eta = g(\xi)$ functions. –c and -d: values of ξ, η, U_x^9, $U_x^0 = E_{xx}(L + 2e_v)$, $U_y^0 = E_{yy}(2H + e_h)$. –a and –c: multi-linear model. –b and –d: Xu-Needleman model.

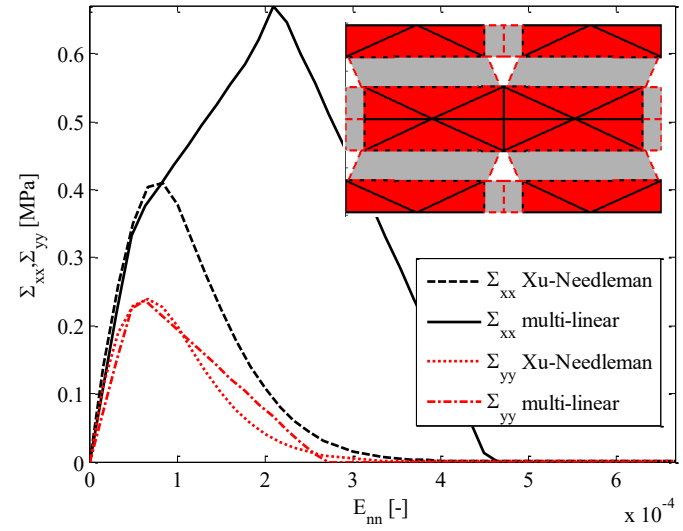

-a

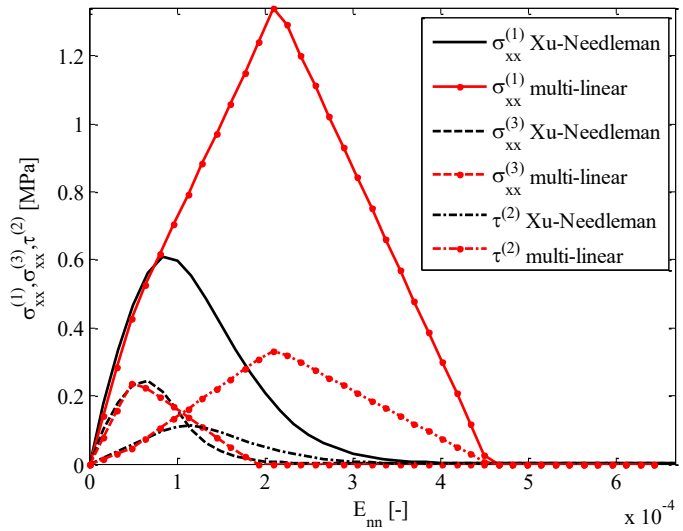

-b

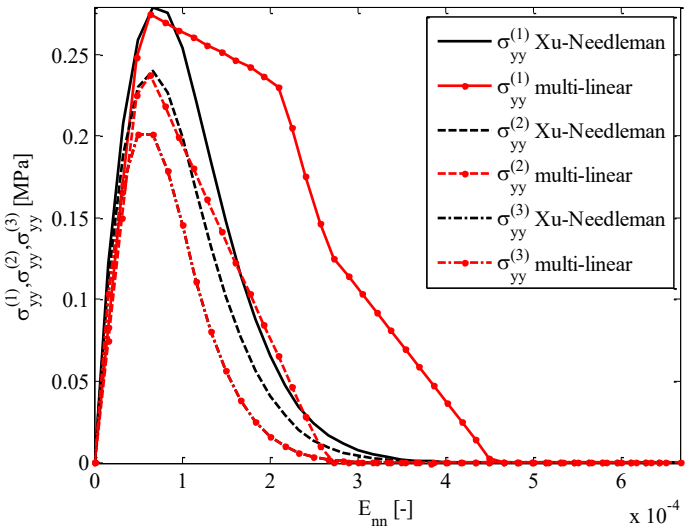

-c

Figure 13: ϑ=45° (inclined direction of the macroscopic strain). Stress-strain curves. –a: Homogenized horizontal (Σ_{xx}) and vertical (Σ_{yy}) stresses. –b: micro stresses $\sigma_{xx}^{(1)}$, $\sigma_{xx}^{(3)}$, $\tau^{(2)}$. –c: micro stresses $\sigma_{yy}^{(1)}$, $\sigma_{yy}^{(2)}$, $\sigma_{yy}^{(3)}$.

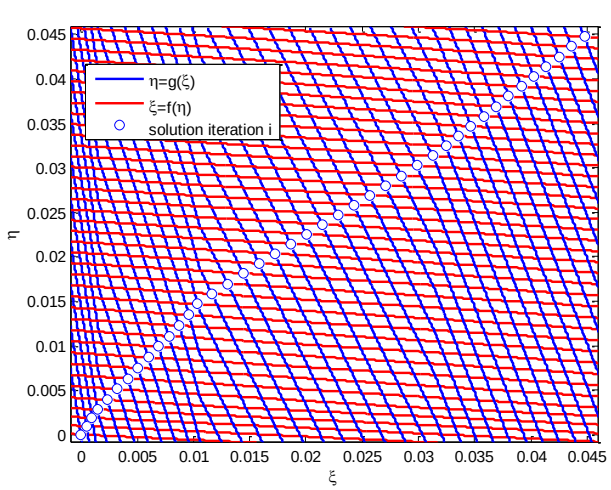

-a

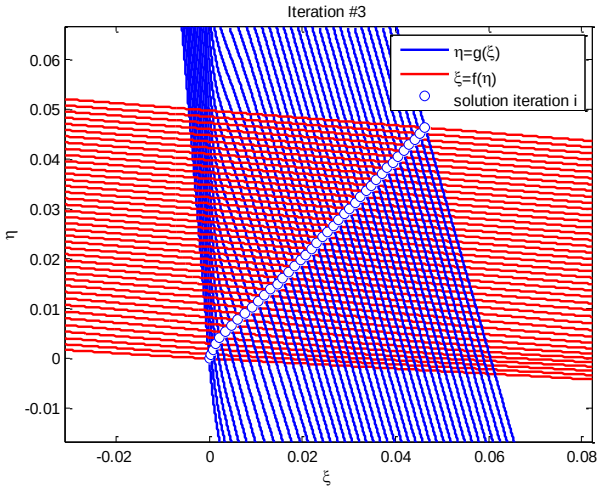

-b

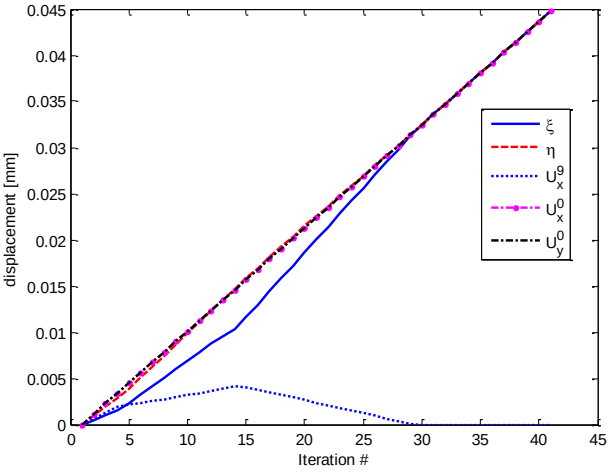

-c

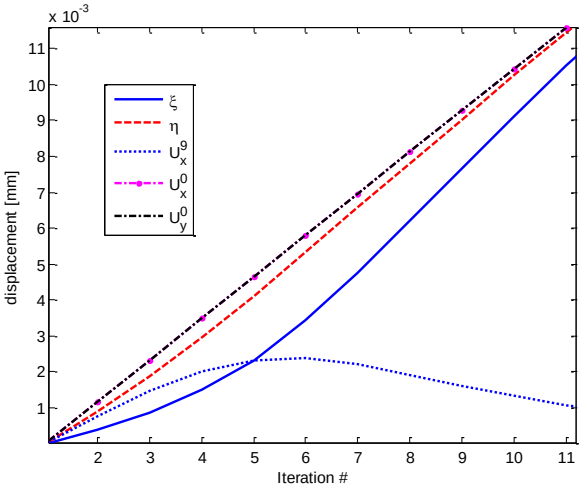

-d

Figure 14: ϑ=45° (inclined direction of the macroscopic strain). Graphical determination of variables ξ and η at different values of applied macroscopic strain. –a and -b: $\xi = f(\eta)$ and $\eta = g(\xi)$ functions. –c and -d: values of ξ, η, U_x^9, $U_x^0 = E_{xx}(L + 2e_v)$, $U_y^0 = E_{yy}(2H + e_h)$. –a and –c: multi-linear model. –b and –d: Xu-Needleman model.

ϑ=15°

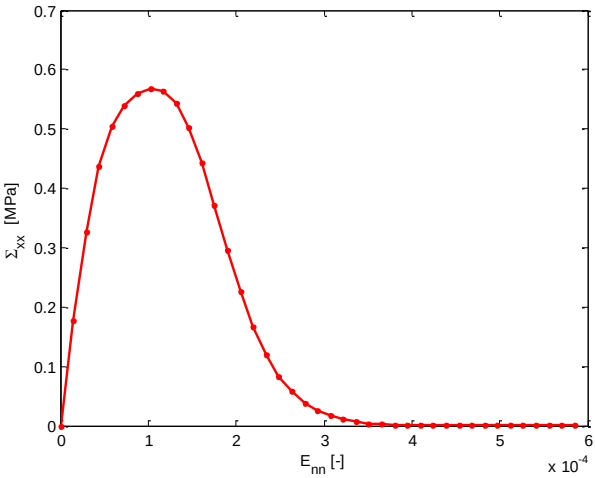

-a

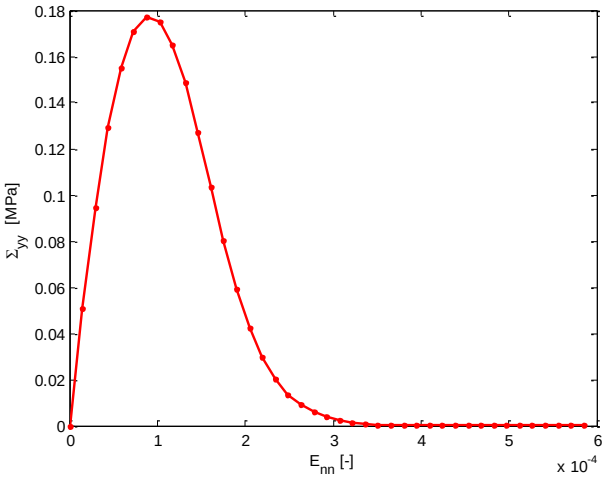

-b

Figure 15: ϑ=15° (inclined direction of the macroscopic strain). Stress-strain curves, Xu-Needleman model. –a: Homogenized horizontal stress Σ_{xx}. –b: Homogenized vertical stress Σ_{yy}.

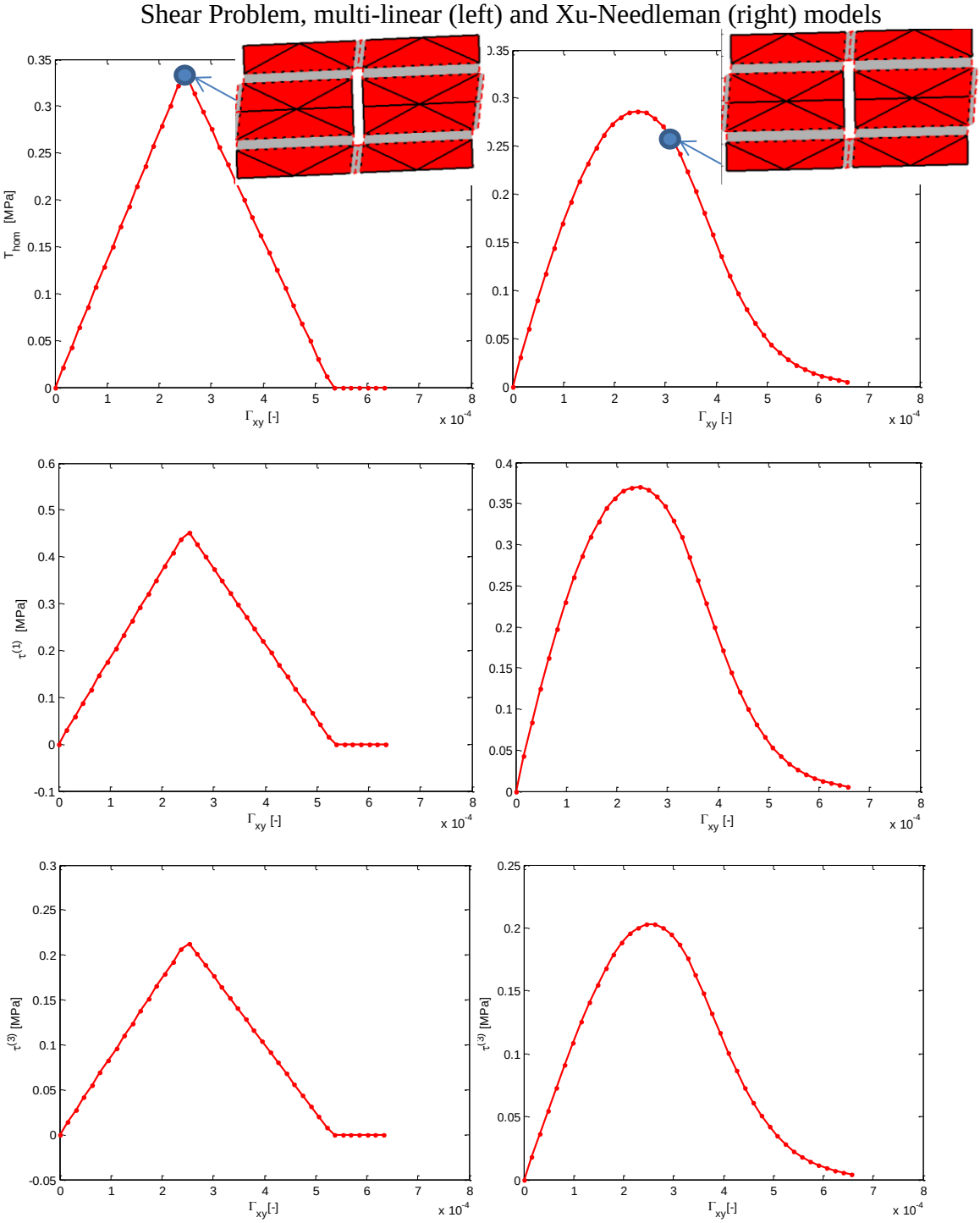

Figure 16: Shear problem. Stress-strain curves, multi-linear (left) and Xu-Needleman (right) models. –a: Homogenized shear stress T_{hom}. –b: Shear stress on element (1) $\tau^{(1)}$. –c: shear stress on element (3) $\tau^{(3)}$.

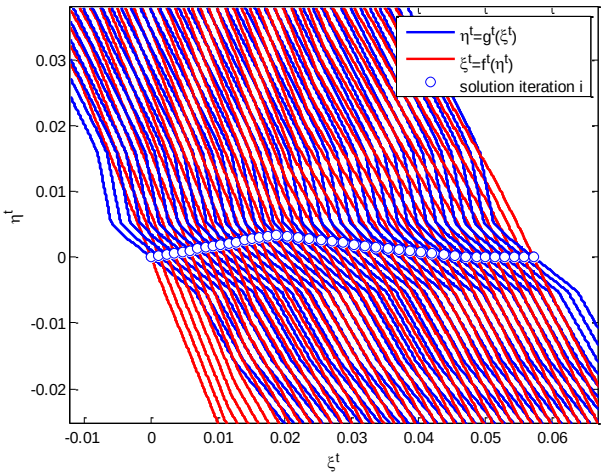

-a

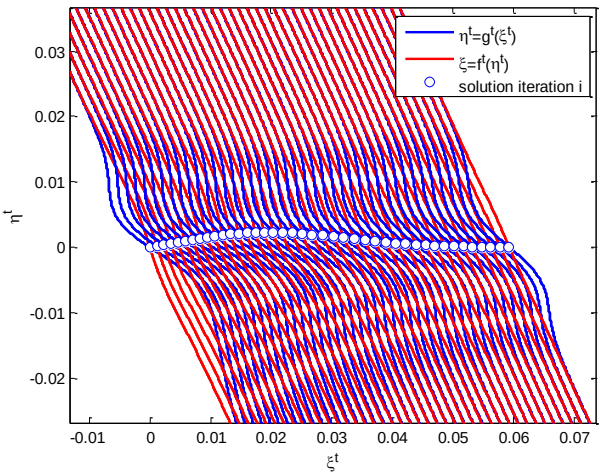

-b

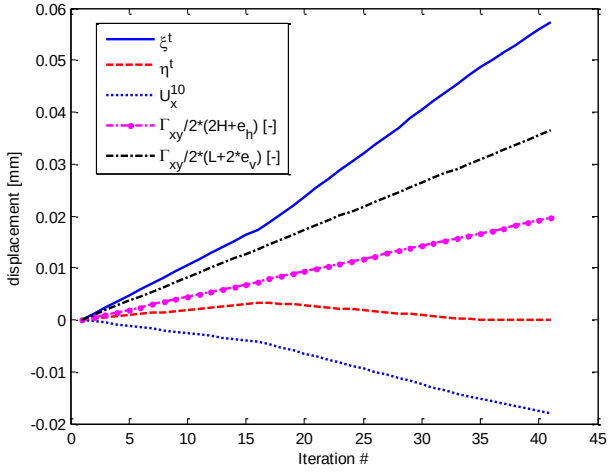

-c

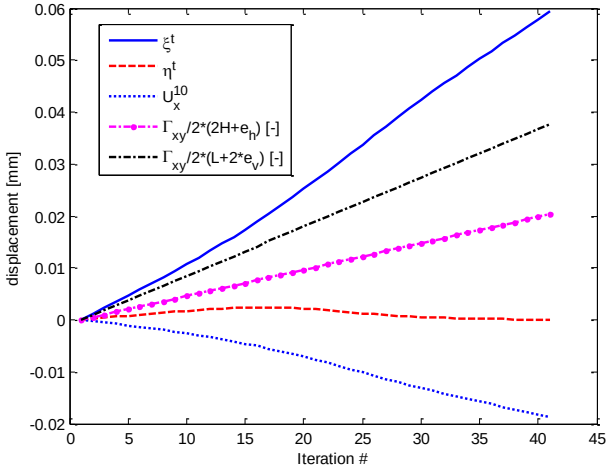

-d

Figure 17: Shear problem, multi-linear model (-a and –c) and Xu-Needleman model (-b and –d). –a and –b: Graphical determination of variables ξ^t and η^t at different values of applied macroscopic strain, $\xi^t = f^t(\eta^t)$ and $\eta^t = g^t(\xi^t)$ functions. –c and -d: values of ξ^t, η^t, U_x^{10}, $\Gamma_{xy}/2(2H+e_h)$, $\Gamma_{xy}/2(L+2e_v)$.

3. Structural level model implementation

Two possible implementations of the semi-analytical homogenization model proposed are possible at structural level, the first is a so-called “nested multi-scale technique” (adopted by Kouznetsova et al. [44] and then applied to the modeling of damage by Massart and co-workers [20]-[22][45] and non-stationary transport processes [46] in masonry), the second is a RBSM (Rigid Body and Spring Model [47]), already used -but without homogenization concepts embedded- by different researchers, among the others Casolo and co-workers [48] [49].

A multi-scale continuum implementation is rigorous, but rather complex to deal with from a computational standpoint. Essentially, such a procedure homogenizes the heterogeneous materials at the meso-scale with the aim of evaluating an average stress-strain response of the unit cell, usually solving a Boundary Value Problem (BVP) on the unit cell by means of FEs. The utilization of softening laws on the unit cell typically exhibits localization in narrow zones. Softening at the meso-scale coupled with a macroscopic local solver is characterized by loss of ellipticity of the governing equations, where the width of the softening band is undetermined at a structural level.

The second procedure is very-straightforward, because obtained by means of a simple discretization with rigid triangular or quadrilateral elements interconnected by axial and shear springs exhibiting softening. The procedure is not new, it is indeed originally due to Kawai [47] who solved a variety of different structural problems, showing how mechanical systems constituted by rigid elements interconnected by (eventually non-linear) springs (RBSM) turn out to provide quite accurate results when compared with FEs.

The efficiency of RBSM in the non-linear static and dynamic analysis of masonry structures is well known from more than two decades, thanks to valuable contributions of different authors (e.g. Casolo and co-workers [48][49]) on conceptually different RBSM models applied to masonry loaded in- and out-of-plane.

The intrinsic advantage of RBSM discretizations applied to homogenization (which is the original contribution of the present paper) within a multi-scale technique is that meso- and macro-scale

problems are fully decoupled. In this way, the implementation of the homogenization model occurs directly at a structural level, without needing a solution at each load step of a non-linear FE homogenization problem for each Gauss-point. The implementation to any robust commercial FE code is therefore very straightforward and in principle does not require interfacing with any User defined MATerial subroutine (UMAT). Non-linearity and softening can be dealt with by means of a very intuitive approach, using exclusively mono-dimensional elements. In addition, the number of variables involved in the discretized structural problems is generally lower than that of classic FEM. The present implementation of the homogenized RBSM code is done within the commercial code Abaqus [42].

Unfortunately the simplicity of RBSM that made it popular in common structural applications is also its relevant limitation in all those problems (as the present one) exhibiting softening of the constituent materials. As a matter of fact, cracks can zigzag only between contiguous rigid elements, thus making such approach intrinsically affected by localization of damage and non-objectivity of the response, with potentially strong mesh dependence.

Whilst such limitation cannot be superseded, it has been however shown that both structured and unstructured meshes are able to provide in the majority of the cases, results quite reliable from an engineering point of view. As a consequence, having in mind the theoretical limitations of RBSM in presence of softening, they are accepted in dealing with common practical applications, where it is preferred efficiency, maintaining the numerical models conceptually simple.

Another remarkable issue of RBSM applied to masonry is that shear and normal behavior are uncoupled. Simplified Mohr-Coulomb relations are usually adopted to rule shear spring strength, to mitigate such further limitations, as in [48][49].

In what follows, some basic features of the two different approaches adopted at a structural level, i.e. “nested multi-scale technique” and “homogenized RBSM”, will be reviewed.

3.1. Nested multi-scale technique

This technique is implemented in a non-commercial Matlab FE code [50] which was previously utilized with a different homogenization model (elasto-plastic with softening) in [16].

The principle of nested multi-scale technique within masonry homogenization is well known from past studies, e.g. by Massart [45], and can be summarized in few steps.

First, a macroscopic strain $\mathbf{E}$ is obtained at each iteration of the nonlinear macroscopic solution procedure for all Gauss points. $\mathbf{E}$ is transferred from the macro- to the meso-scale (unit cell) in the so-called meso/macro-scale transition. The macroscopic stress tensor $\boldsymbol{\Sigma}$ is then found solving the homogenization problem and transferred again to the macro-scale until convergence at each iteration step. The meso-macro transition also permits to extract the constitutive tangent, relating variations of $\boldsymbol{\Sigma}$ to variations of $\mathbf{E}$.

Since the constitutive relationship of the interfaces is holonomic (hence a total strain formulation is adopted), local unloading in some Gauss points (which is possible even in monotonic static analyses) cannot be correctly reproduced with the approach proposed, but it has been shown that globally such limitation has not meaningful effects.

Apart some numerical routines that the FE code used should own to deal with softening (such as a robust arc-length routine), mesh objectivity is a controversial issue, i.e. the requirement that the results are unaffected by the adopted discretization.

In a strain-softening material, strain tends to localize into a narrow zone where energy is dissipated according to its size, while outside the continuum unloads elastically. If standard local models are used (i.e. the material response is computed as a function of local strains), localization is related to the finite element dimension. As a rule, in presence of softening, the band where dissipation occurs coincides with only one strip of elements through the mesh. This outcome could be also technically acceptable, however the energy of dissipation is proportional to the size of the finite elements, thus going down as the elements become smaller and smaller upon mesh refinement. In such cases, non-objective results depending on the FE size are obtained.

The strategy adopted here to circumvent this problem is simply to approximate in tension the horizontal and vertical homogenized stress-strain curves with an exponential softening (least square approximation) and adopt exactly the same procedure proposed by Lourenço and co-workers in [3] to achieve mesh objectivity, i.e. scaling the fracture energies by means of the equivalent length $\bar{h}$ defined as:

$$\bar{h} = \alpha_h \sqrt{A_e} = \alpha_h \left(\sum_{\xi=1}^{n_\xi} \sum_{\eta=1}^{n_\eta} \det J w_\xi w_\eta \right) \quad (14)$$

Where w_ξ, w_η are weight factors of the Gaussian integration scheme, J the Jacobian of the transformation, A_e the element area and α_h a modification factor which is equal to 1 for quadratic elements and $\sqrt{2}$ for linear elements.

It is indeed possible to avoid the quite cumbersome procedure proposed in [45], because the BVP at the mesoscale is solved without the need of a FE discretization, but in "quasi" analytical form.

3.2. Homogenized RBSM model

In Abaqus [42], RBSM is implemented using plate and shell elastic elements with high Young modulus (to approximate the hypothesis of infinite stiffness) and shear and normal springs interconnecting contiguous elements.

The mechanical model adopted for the springs is a Concrete Damage Plasticity (CDP) one, already available in the standard versions of Abaqus. Values to assign to different parameters are those to match exactly the elastic, peak and post peak behavior provided by the holonomic homogenization model. Each interface, depending on its orientation with respect to masonry material axes, has its own characteristics and therefore requires different CDP mechanical parameters to tune. Apart the simplicity of implementation (which requires only the availability of a standard non-linear FE commercial code), noticeable advantages are the possibility to consider masonry orthotropy in the inelastic range and –thanks to the utilization of a damage plasticity model- the possible generalization to non-linear dynamic loads. Finally, the extension to out-of-plane loads and the

study of vaults and domes is in principle very straightforward. On the other hand, the strong limitation of an almost fully uncoupled behavior between shear and normal actions is worth mentioning, because the role played by vertical pre-compression can be taken into account in the model only in an approximate way, i.e. increasing springs tangential strength with respect to the level of vertical pre-compression.

The most general implementation of RBSM requires the utilization of unstructured meshes. Indeed, for complex geometries, auto-meshing routines are usually needed to deal with geometric irregularities. Therefore, and this is the approach classically adopted by Kawai [47], triangular elements should be preferred. Hereafter, however, we will refer in general to rigid elements that can be either triangular or quadrilateral with irregular shape, as sketched in Figure 18-a.

The mechanical properties of the springs connecting two contiguous rigid elements are typically set equating the stored elastic energy in the RBSM discretization to that of the elastic continuum. In case of homogenized masonry, the continuum is orthotropic.

Two contiguous rigid elements with a common edge Γ_{12} (length equal to L_{12}) are considered. They are thought as interconnected by two axial (shear) springs with the same stiffness k_n (k_t).

Langrangian variables of a rigid element M are centroid displacements (u_x^M and u_y^M) and rotation Φ_z^M around centroid, all collected into vector $\mathbf{U}_M^T = [\, u_x^M \,;\, u_y^M \,;\, \Phi_z^M \,]$.

Displacement field of points on the edge Γ_{12} are provided by the following trivial formula:

$$\begin{bmatrix} u_{x0} \\ u_{y0} \end{bmatrix} = \begin{bmatrix} 1 & 0 & -(y_0 - y_M) \\ 0 & 1 & (x_0 - x_M) \end{bmatrix} \begin{bmatrix} u_x^M \\ u_y^M \\ \Phi_z^M \end{bmatrix} = \mathbf{R}_M(\mathbf{P}_0)\mathbf{U}_M \qquad (15)$$

Where x_0 and y_0 are the coordinates of $\mathbf{P}_0$ point on Γ_{12} edge and u_{x0} (u_{y0}) is the horizontal (vertical) displacement of the point.

Indicating with $\mathbf{s}^e$ ($\mathbf{r}^e$) the unitary vector parallel (perpendicular) to Γ_{12}, the transformation matrix from the global to the interface local coordinate system is:

$$\begin{bmatrix} \mathbf{s}^e \\ \mathbf{r}^e \end{bmatrix} = \begin{bmatrix} \mathbf{s}^e \bullet \mathbf{e}_1 & \mathbf{s}^e \bullet \mathbf{e}_2 \\ \mathbf{r}^e \bullet \mathbf{e}_1 & \mathbf{r}^e \bullet \mathbf{e}_2 \end{bmatrix} \begin{bmatrix} \mathbf{e}_1 \\ \mathbf{e}_2 \end{bmatrix} = \mathbf{T} \begin{bmatrix} \mathbf{e}_1 \\ \mathbf{e}_2 \end{bmatrix} \Leftrightarrow \begin{bmatrix} \mathbf{e}_1 \\ \mathbf{e}_2 \end{bmatrix} = \mathbf{T}^{-1} \begin{bmatrix} \mathbf{s}^e \\ \mathbf{r}^e \end{bmatrix} \tag{16}$$

where the symbol $\bullet$ indicates the internal product.

The jump of displacements on the interface Γ_{12} between M and N turns out therefore to be:

$$[\mathbf{u}^{M-N}] = \begin{bmatrix} \Delta u_n \\ \Delta u_t \end{bmatrix} = \mathbf{T}^{-1} \left[\mathbf{R}_M (\mathbf{P}_0) \mathbf{U}_M - \mathbf{R}_N (\mathbf{P}_0) \mathbf{U}_N \right] \tag{17}$$

where Δu^r and Δu^s are the normal and tangential jumps of displacement on the interface, respectively.

Assuming the elastic energy equivalence between the discrete RBSM model and the orthotropic continuum, from relation (17), it can be easily shown applying the Castigliano's theorem and separately to the mechanical systems $\Delta u^r \neq 0$ and $\Delta u^s \neq 0$, that the axial and shear stiffnesses of the interface springs are:

$$k_n = \frac{E_{nn}}{2\left(1 - \nu_{xy}\nu_{yx}\right)\left(h_1 + h_2\right)}$$

$$k_t = \frac{G_{nt}}{\left(h_1 + h_2\right)} \tag{18}$$

The formula is conceptually identical for triangular and quadrilateral elements, with h_1 and h_2 meaning shown in Figure 18-a. The utilization of triangular elements in RBSM would be preferable, because crack propagation can occur along inclined lines, especially for unstructured meshes, but even the utilization of quadrilateral elements proved good performance in the non-linear range [48].

E_{nn} and G_{nt} are estimated once the elastic orthotropic behavior of the homogenized material is known, according to results shown in Figure 8.

Elastic and inelastic behavior of a homogenized interface having normal $\mathbf{n} = \begin{bmatrix} n_x & n_y \end{bmatrix}^T$ and direction $\mathbf{t} = \begin{bmatrix} -n_y & n_x \end{bmatrix}^T$ is found assuming that the interface is subjected to the following homogenized strains:

$$\begin{bmatrix} \bar{\varepsilon}_{tt}=0 \\ \bar{\varepsilon}_{nn} \\ \bar{\varepsilon}_{nt} \end{bmatrix} = \begin{bmatrix} E_{xx}n_y^2 + E_{yy}n_x^2 - \Gamma_{xy}n_x n_y \\ E_{xx}n_x^2 + E_{yy}n_y^2 + \Gamma_{xy}n_x n_y \\ -E_{xx}n_x n_y + E_{yy}n_x n_y + \frac{1}{2}\Gamma_{xy}\left(n_x^2 - n_y^2\right) \end{bmatrix} \tag{19}$$

From (19), to directly find the homogenized elastic modulus E_{nn} along $\mathbf{n}$, we further impose $\bar{\varepsilon}_{nt}$=0, which trivially corresponds to applied boundary displacements on the unit cell in such a way that:

$$\begin{aligned} \Gamma_{xy} &= E_{xx}\frac{n_y}{n_x} + E_{yy}\frac{n_x}{n_y} \\ E_{yy} &= E_{xx}\left(\frac{n_y}{n_x}\right)^2 \end{aligned} \tag{20}$$

Similar considerations are made for the determination of G_{nt}, assuming in such a case $\bar{\varepsilon}_{nn}$=0.

Equation (20) allows to tune both the elastic and inelastic behavior of the homogenized interface with normal $\mathbf{n}$. A detailed description of the technical passages adopted to identify spring stiffness (elastic part) in the RBSM model from masonry elastic moduli found at the meso-scale can be found in [43][51]. Inelastic behavior is scaled accordingly to the elastic part, again following [43][51], where the reader is referred for a comprehensive discussion.

For benchmark purposes in the elastic range, the windowed panel studied in the inelastic range in the following Section is here modeled in the elastic range by means of (a) continuum quadrilateral finite elements, (b) rectangular and (c) quadrilateral irregular RBSM meshes with increasing refinement. The masonry material is orthotropic, according to the elastic properties of joints and bricks assumed in the sequel. The convergence of the RBSM meshes upon mesh refinement to the elastic solution found with classic orthotropic FEs is depicted in Figure 18-b ($U_x^{P,FEM}$ is the horizontal displacement of the top edge of the panel found with a FE mesh constituted by 1000 rectangular finite elements).

It is finally interesting to notice that, when the RBSM model is constituted by rigid rectangular elements linked by normal and shear springs at the interfaces, with interface either vertical or horizontal, only $E_{xx}-\Sigma_{xx}$, $E_{yy}-\Sigma_{yy}$ and $\Gamma_{xy}-T_{xy}$ homogenized relationships are needed to tune

normal and shear springs, without the need to obtain homogenized stress-strain relationships along inclined interfaces. The disadvantage is obviously a certain mesh dependence of the result, as it is shown hereafter. The static implementation adopted uses either standard arc-length or displacement based procedures, depending on the available implementation of the commercial code used. Finally, the discrete formulation adopted allows for an easy extension to the non-linear dynamic case.

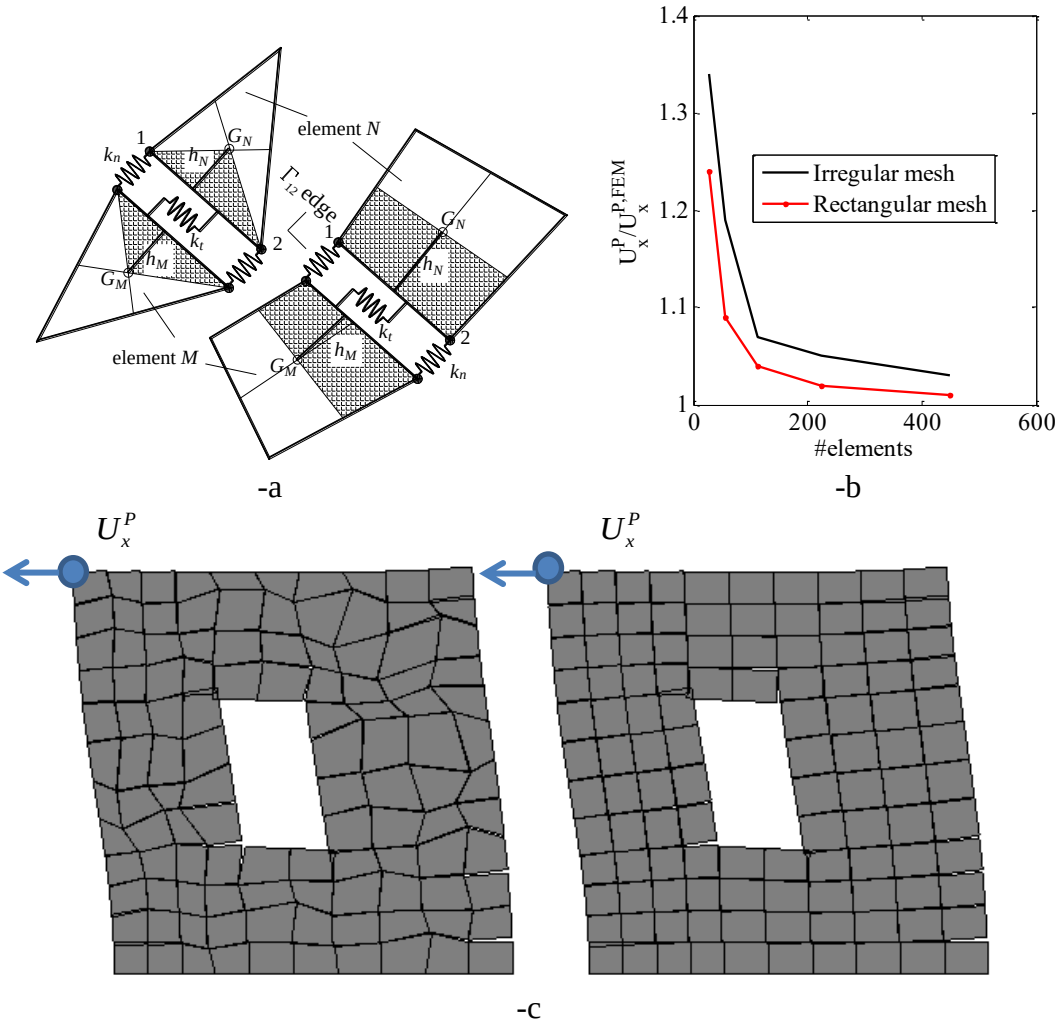

Figure 18: -a: general procedure adopted to tune shear and normal interface springs in RBSM with irregular mesh- -b: performance of unstructured and structured meshes in the elastic stiffness evaluation of the windowed panel analyzed in the paper. .-c elastic deformed shapes obtained with one unstructured and one regular rigid element mesh.

3.3. Validation on a windowed shear panel

The structural simulations performed as benchmark refer to a set of windowed panels experimentally tested in [39]. The homogenized behavior utilized for the interfaces is that discussed

in the previous section. A multi-linear model for joints is assumed in the structural simulations for the sake of simplicity, but very similar results are obtained in the Xu-Needleman case.

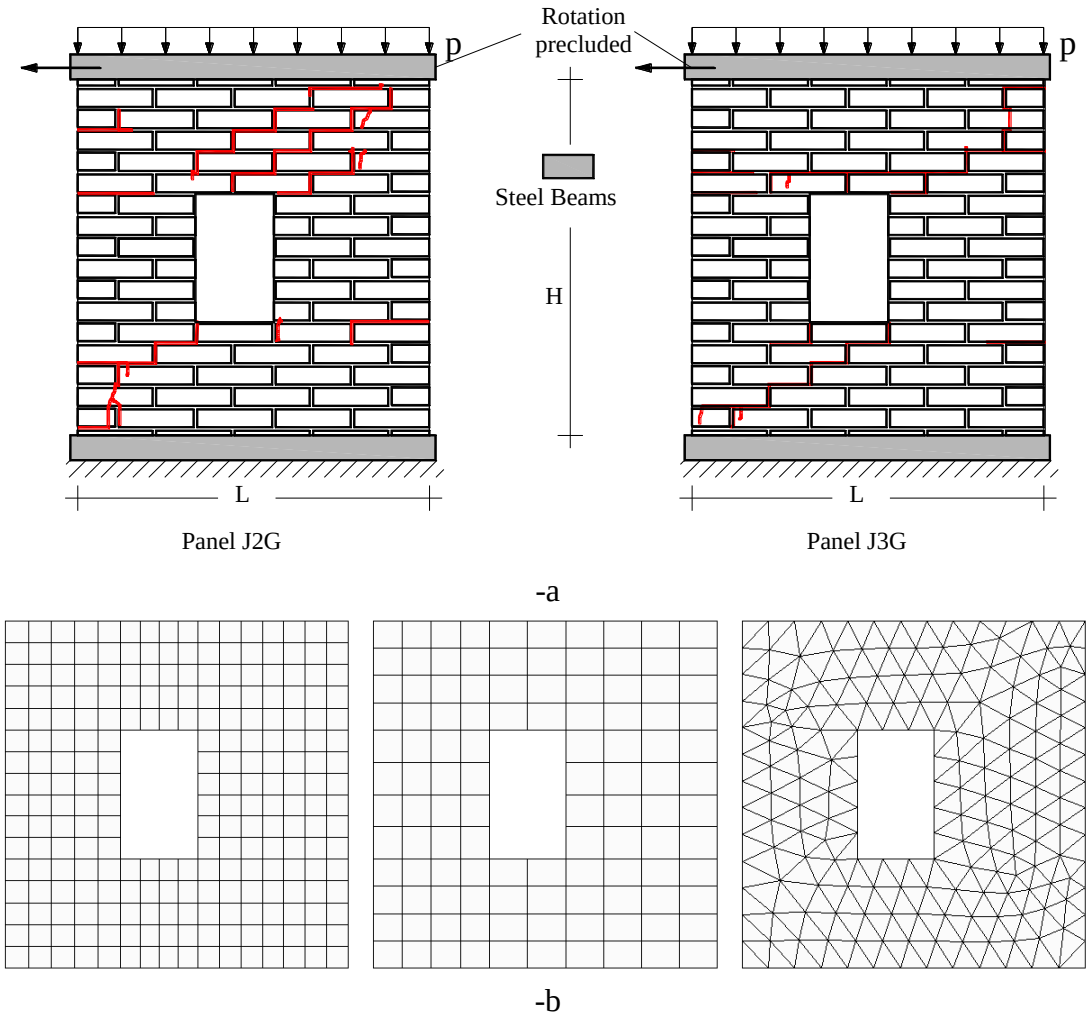

Figure 19: Windowed masonry shear wall by Raijmakers and Vermeltfoort. Geometry (-a) and (-b) meshes utilized (left: RBSM rectangular structured; center: nested multi-scale; right: RBSM triangular unstructured).

Experimentally, two identical walls were tested, labeled as J2G and J3G. The width/height ratio (L/H) of the shear walls is 990 /1000 ([mm]/[mm]); the panels were built up with 18 courses of bricks, from which 16 courses were active and 2 were clamped in stiff steel beams, Figure 19. A vertical pre-compression of 0.3 N/mm^2 was applied on the top and its resultant was kept constant during the complete loading procedure. The stiff steel beam did not allow rotations of the top and was subsequently pushed with an increasing horizontal force. The central opening defines two small relatively weak piers and forces the compressive strut that develops under horizontal loading to spread around both sides of the opening.

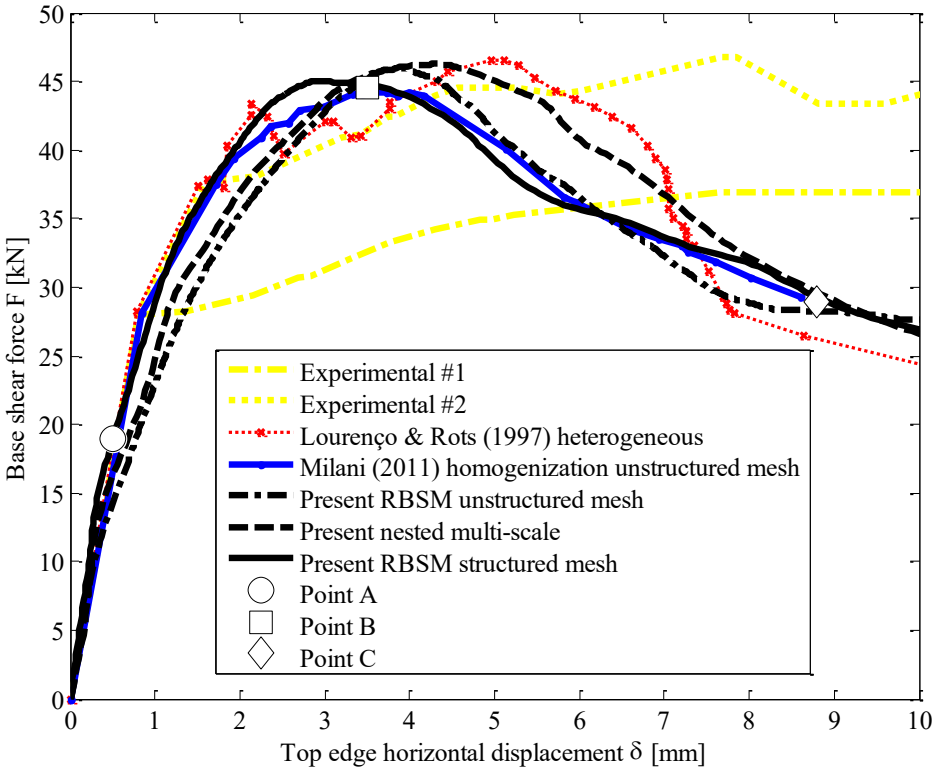

Figure 20: Windowed masonry shear wall by Raijmakers and Vermeltfoort. Comparison among external load-horizontal displacement provided by the present model, previously presented numerical approaches and experimental behavior.

The experimental crack patterns as reported in [39] are illustrated in Figure 19-a. Diagonal zigzagging cracks arose initially from two corners of the opening at four possible locations. Shortly afterwards, tensile cracks arose from the outside of the wall at the base and top of the small piers. Under increasing deformation, predominant diagonal cracks occurred, leading to partial closing of the cracks that were open before. Finally, a collapse mechanism formed with failure of the compressed toes, located at the bottom and top of the wall and at the bottom and top of the small piers.

Meshes used for the non-linear structural analyses are depicted in Figure 19-b. In particular, one RBSM rectangular structured mesh (left), one nested multi-scale (center) and one RBSM triangular unstructured (right) discretization are adopted, in order to have an insight into the possible mesh dependence of the result obtained by means of the rectangular RBSM structured mesh. In all cases,

a medium size discretization is adopted, in order to speed up computations without losing numerical accuracy.

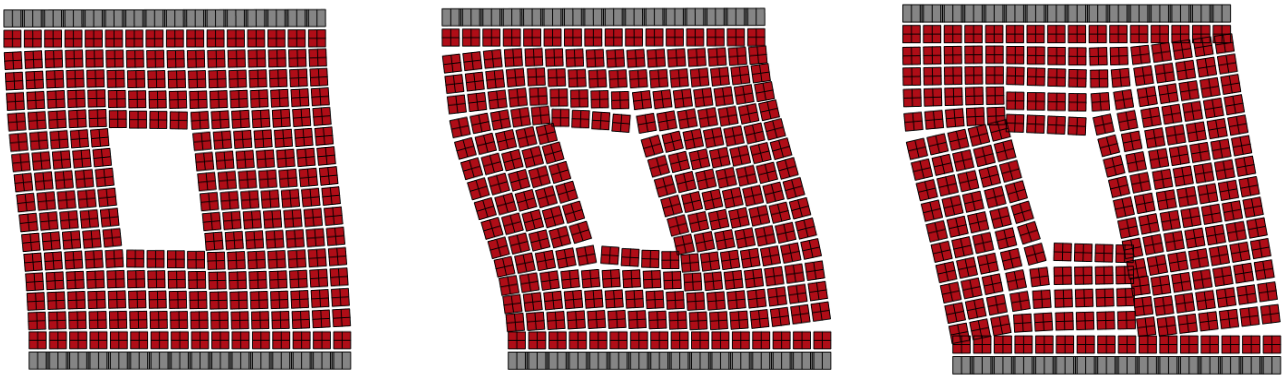

A B C

Figure 21: Deformed shape at different time steps: a- elastic phase, b- peak load, b- end of the simulation (magnified 100 times in A and B, and 10 times in C)

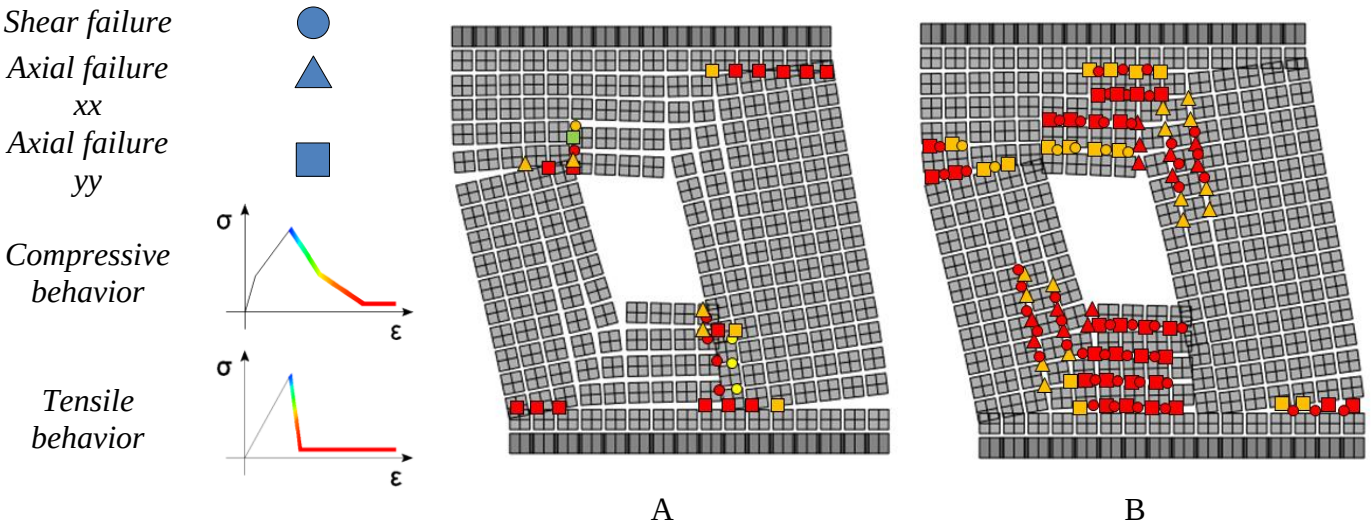

Figure 22: Results provided with the present model: a- damage map in compression, b- damage map in tension, at the end of the simulation

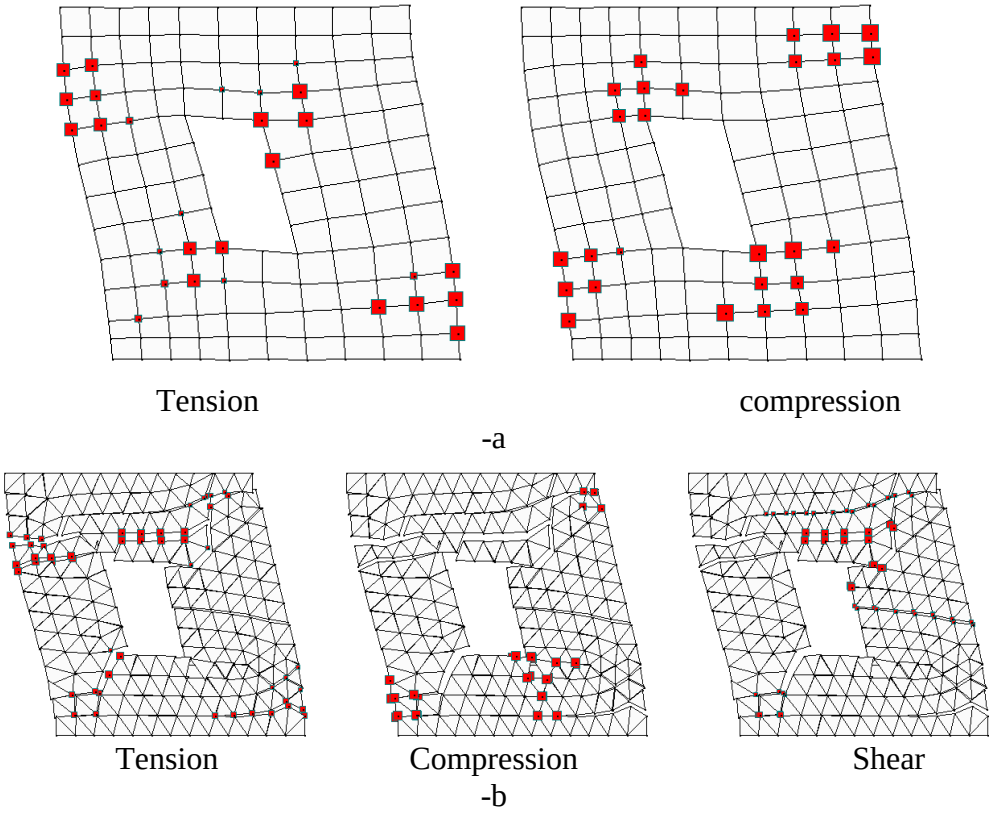

Figure 23: deformed shapes at collapse, with indication of damage. –a: nested multi-scale approach. –b: RBSM approach with unstructured mesh.

Mechanical properties assumed for the constituent materials are summarized in Table I and are taken in agreement with both experimental data provided by Raijmakers and Vermeltfoort [39] (where available) and Lourenço [5] [30], where the same numerical analyses were performed within a heterogeneous approach.

In Figure 20, a comparison among external shear load-horizontal displacement provided by the present model, previously presented numerical approaches [5] [16] [30] and experimental data is depicted. As can be observed, the model proposed seems to provide very satisfactory results, both using a RBSM and a nested multi-scale approach. It is also interesting to notice that the presence of rectangular rigid elements in the RBSM structured mesh seems not to represent a strong limitation for the formation of a reasonable failure mechanism, as can be observed by the three deformed shapes at instants A-C (indicated in the pushover curve of the RBSM structured mesh in Figure 20, A: elastic, B: peak, C: failure) depicted in Figure 21. However, since inelastic deformations are allowed only on pre-assigned crack lines –dependent on the initial mesh- unavoidable mesh dependence is still present especially in the softening branch (as demonstrated by the deviations exhibited by the unstructured RBSM mesh when compared with nested multi-scale response). As a consequence, particular care is recommended in the meshing phase, in order to avoid a drastic overestimation of the load carrying capacity of the structure or a fictitious damage concentration on some interfaces. Figure 22 and Figure 23 finally illustrate damage maps obtained at the end of the numerical analyses. Figure 22 refers to the RBSM structured mesh: circles indicate shear failure, triangles axial horizontal failure and squares axial vertical failure. Figure 23 finally shows on the obtained deformed shapes damage patterns for the nested multi-scale approach (-a) and the RBSM unstructured mesh (-b). Damage is represented with a red square, the dimension indicating its amount. In the nested multi-scale approach it is obviously not possible a distinction between normal and shear damage, being the procedure native 2D (only damage in tension and compression can be distinguished), whereas in the unstructured RBSM approach three sub-figures are utilizing, separating normal damage in tension, compression and shear damage.

Comparing all the results obtained (deformed shapes and crack patterns), it can be concluded that all the numerical models proposed show common features, with the formation of failure mechanisms fully in agreement with experimental evidences, i.e. diagonal cracks propagation on

two opposite corners of the central window and tension crack opening/compression crushing of the two piers, that clearly exhibit a rocking failure with rotation around the compressed toe.

4. Conclusions

A quasi-analytical simplified compatible homogenization model accounting for the softening behavior of mortar joints in the case of in-plane loads has been presented. In the first step, a rectangular elementary cell has been discretized by means of a few triangular elastic FEs and non-linear joints reduced to interfaces. Homogenized stress-strain diagrams have been found by means of a quasi-analytical approach, where kinematic variables are found graphically at each imposed external macroscopic strain. The procedure allows a direct estimation of displacements in the unit cell, since a holonomic behavior of mortar is assumed. The second step (structural level) is performed by means of rigid quadrilateral elements interconnected by holonomic shear-nornal springs, where all the non-linearity is concentrated and with mechanical properties directly determined from the homogenization problem. The main innovative aspects of the numerical model proposed are twofold. At a cell level, the FE discretization adopted allows for a quasi-analytical determination of the homogenized stress-strain behavior of running bond masonry. At a structural level, the procedure can be directly implemented into any general purpose FE commercial code (either using elasto-damaging 2D elements or rigid elements interconnected by elasto-damaging springs), because it does not require the recursive solution of a homogenization problem in each Gauss point at each load step.

5. Acknowledgements

The present investigation was developed within the activities of the (Italian) University Network of Seismic Engineering Laboratories–ReLUIS in the research program funded by the Italian Civil Protection National Service – Progetto Esecutivo 2015 – Research Line ‘‘Masonry Structures”, WP2-WP4.

6. References

[1] Di Pasquale S. New trends in the analysis of masonry structures. Meccanica 1992; 27: 173-184.

[2] Berto L, Saetta A, Scotta R, Vitaliani R. An orthotropic damage model for masonry structures. Int J Numer Methods Engng 2002; 55: 127–57.

[3] Lourenço PB, de Borst R, Rots JG. A plane stress softening plasticity model for orthotropic materials. International Journal for Numerical Methods in Engineering 1997; 40: 4033-4057.

[4] Milani G. Four approaches to determine masonry strength domain. Proceedings of ICE, Engineering and Computational Mechanics 2015; 168(3): 99-121.

[5] Lourenço PB, Rots J. A multi-surface interface model for the analysis of masonry structures. Journal of Engineering Mechanics ASCE 1997; 123 (7): 660-668.

[6] Macorini L, Izzuddin BA. A non-linear interface element for 3D mesoscale analysis of brick-masonry structures. International Journal for Numerical Methods in Engineering 2010; 85(12): 1584–1608.

[7] Lotfi HR, Shing PB. Interface model applied to fracture of masonry structures. Journal of Structural Engineering ASCE 1994; 120 (1): 63-80.

[8] Sutcliffe DJ, Yu HS, Page AW. Lower bound limit analysis of unreinforced masonry shear walls. Computers & Structures 2001; 79: 1295-1312.

[9] Macorini L, Izzuddin BA. Nonlinear analysis of masonry structures using mesoscale partitioned modelling. Advances in Engineering Software 2013; 60-61: 59-69.

[10] Pietruszczak S, Ushaksarei R. Description of inelastic behaviour of structural masonry. International Journal of Solids and Structures 2003; 40: 4003–19.

[11] Gambarotta L, Lagomarsino S. Damage models for the seismic response of brick masonry shear walls. Part I: the mortar joint model and its applications. Earthquake Engineering and Structural Dynamics 1997; 26: 423–439.

[12] de Buhan P, de Felice G. A homogenisation approach to the ultimate strength of brick masonry. Journal of the Mechanics and Physics of Solids 1997; 45 (7): 1085-1104.

[13] Lopez J, Oller S, Onate E, Lubliner J. A homogeneous constitutive model for masonry. International Journal for Numerical Methods in Engineering 1999; 46(10): 1651–1671.

[14] Luciano R, Sacco E. Homogenisation technique and damage model for old masonry material. International Journal of Solids and Structures 1997; 34 (24): 3191-3208.

[15] Pegon P, Anthoine A. Numerical strategies for solving continuum damage problems with softening: application to the homogenisation of masonry. Computers & Structures 1997; 64 (1-4): 623-642.

[16] Milani G. Simple homogenization model for the non-linear analysis of in-plane loaded masonry walls. Computers & Structures 2011; 89: 1586–1601.

[17] Milani G, Lourenço PB, Tralli A. Homogenised limit analysis of masonry walls. Part I: failure surfaces. Computers & Structures 2006; 84(3-4): 166-180.

[18] Milani G, Lourenço PB, Tralli A. Homogenization approach for the limit analysis of out-of-plane loaded masonry walls. Journal of Structural Engineering ASCE 2006; 132(10): 1650-1663.

[19] Milani G, Lourenço PB. Monte Carlo homogenized limit analysis model for randomly assembled blocks in-plane loaded. Computational Mechanics 2010; 46(6): 827-849.

[20] Massart T, Peerlings RHJ, Geers MGD. Mesoscopic modeling of failure and damage-induced anisotropy in brick masonry. Eur J Mech A/Solids 2004; 23:719–35.

[21] Massart T, Peerlings RHJ, Geers MGD. An enhanced multi-scale approach for masonry wall computations with localization of damage. International Journal for Numerical Methods in Engineering 2007; 69: 1022–1059.

[22] Mercatoris BCN, Massart T. A coupled two-scale computational scheme for the failure of periodic quasi-brittle thin planar shells and its application to masonry. International Journal for Numerical Methods in Engineering 2011; 85(9): 1177–1206.
[23] Colliat JB, Davenne L, Ibrahimbegovic A, Modélisation jusqu'à rupture de murs en maçonnerie chargés dans leur plan. Revue francaise de génie civil 2002; 4: 593-606.
[24] Xu XP, Needleman A. Void nucleation by inclusion debonding in a crystal matrix. Modell. Simulation Mater. Sci. Eng. 1993; 2:417-418.
[25] McGarry P, Máirtín EO, Parry G, Beltz GE. Potential-based and non-potential-based cohesive zone formulations under mixed-mode separation and over-closure. Part I: Theoretical analysis. Journal of the Mechanics and Physics of Solids 2014; 63: 336–362.
[26] Fedele R. Simultaneous Assessment of mechanical properties and boundary conditions based on Digital Image Correlation. Experimental Mechanics 2015; 55(1): 139-153.
[27] Suquet P. Analyse limite et et homogeneisation. Comptes Rendus de l'Academie des Sciences - Series IIB – Mechanics 1983; 296: 1355-1358.
[28] Cecchi A., Milani G., Tralli A. A Reissner-Mindlin limit analysis model for out-of-plane loaded running bond masonry walls. International Journal of Solids and Structures 2007; 44(5): 1438-1460.
[29] Drougkas A, Roca P, Molins C. Analytical micro-modeling of masonry periodic unit cells – Elastic properties. International Journal of Solids and Structures 2015; 69-70: 169-188.
[30] Lourenço PB. Computational strategies for masonry structures. PhD Thesis. TU Delft, The Netherlands, 1996.
[31] Lourenço P.B. On the use of homogenisation techniques for the analysis of masonry structures. Masonry Int 1997; 11(1):26-32.
[32] Pietruszczak S, Niu X. A mathematical description of macroscopic behavior of brick masonry. International Journal of Solids and Structures 1992; 29(5):531-546.
[33] Taliercio A. Closed-form expressions for the macroscopic flexural rigidity coefficients of periodic brickwork. Mechanics Research Communications 2016; 72: 24-32.
[34] Pande GN, Liang JX, Middleton J. Equivalent elastic moduli for brick masonry. Comput Geotech 1989; 8:243-65.
[35] Anthoine A. Derivation of the in-plane elastic characteristics of masonry through homogenization theory. International Journal of Solids and Structures 1995; 32(2): 137-163.
[36] Pegon P, Anthoine A. Numerical strategies for solving continuum damage problems with softening: application to the homogenisation of masonry. Comput Struct 1997; 64(1-4):623-42.
[37] Mistler M, Anthoine A, Butenweg C. In-plane and out-of-plane homogenisation of masonry. Comput Struct 2007; 85(17-18):1321-30.
[38] Cecchi A, Milani G, Tralli A. Validation of analytical multiparameter homogenization models for out-of-plane loaded masonry walls by means of the finite element method. ASCE J Eng Mech 2005; 131(2):185-98.
[39] Raijmakers TMJ, Vermeltfoort A. Deformation controlled tests in masonry shear walls (in Dutch). Report B-92-1156, TNO-Bouw, Delft, The Netherlands, 1992.
[40] Pelà L, Cervera M, Roca P. An orthotropic damage model for the analysis of masonry structures. Construction and Building Materials 2013; 41: 957-967.
[41] Casolo S, Milani G. A simplified homogenization-discrete element model for the non-linear static analysis of masonry walls out-of-plane loaded. Engineering Structures 2010; 32: 2352-2366.
[42] ABAQUS™. Theory manual, version 6.6; 2006.
[43] Bertolesi E, Lourenço PB, Milani G. Simple total displacement non-linear homogenization approach: Implementation on commercial FEM and validation. In preparation.

[44] Kouznetsova V, Geers M, Brekelmans M. Multi-scale constitutive modelling of heterogeneous materials with a gradient-enhanced computational homogenization scheme. International Journal for Numerical Methods in Engineering 2002; 54(8): 1235-1260.
[45] Massart TJ. Multi-scale modeling of damage in masonry structures. PhD Thesis. TU Eindhoven, Eindhoven, The Netherlands 2003.
[46] Sỳkora J, Krejčí T, Kruis J, Šejnoha M. Computational homogenization of non-stationary transport processes in masonry structures. Journal of Computational and Applied Mathematics 2011; 236(18): 4745-4755.
[47] Kawai T. New discrete models and their application to seismic response analysis of structures. Nucl. Eng. Des. 1978; 48: 207–229.
[48] Casolo S, Pena F. Rigid element model for in-plane dynamics of masonry walls considering hysteretic behaviour and damage. Earthquake Engineering and Structural Dynamics 2007; 36(8): 1029-1048.
[49] Casolo S. Modelling in-plane micro-structure of masonry walls by rigid elements. International Journal of Solids and Structures 2004; 41(13): 3625-3641.
[50] Matlab™. Matlab's Users' Guide version R2017a, The Mathworks; 2017.
[51] Bertolesi E. Simple compatible homogenisation strategies. Application to unreinforced and FRCM reinforced masonry structures in and out of plane loaded. PhD Thesis, Technical University of Milan, Milan (Italy), 2017.